Megalencephalic leukoencephalopathy with subcortical cysts protein 1 regulates glial surface localization of GLIALCAM from fish to humans

Sirisi, Sònia ; Folgueira, Mónica ; López-Hernández, Tania ; Minieri, Laura ; Pérez-Rius, Carla ; Gaitán-Peñas, Héctor ; Zang, Jingjing ; Martínez, Albert ; Capdevila-Nortes, Xavier ; De La Villa, Pedro ; Roy, Upasana ; Alia, A ; Neuhauss, Stephan ; Ferroni, Stefano ; Nunes, Virginia ; Estévez, Raúl ; Barrallo-Gimeno, Alejandro

Abstract: Megalencephalic leukoencephalopathy with subcortical cysts (MLC) is a leukodystrophy characterized by myelin vacuolization and caused by mutations in MLC1 or GLIALCAM. Patients with recessive mutations in either MLC1 or GLIALCAM show the same clinical phenotype. It has been shown that GLIALCAM is necessary for the correct targeting of MLC1 to the membrane at cell junctions, but its own localization was independent of MLC1 in vitro. However, recent studies in Mlc1(-/-) mice have shown that GlialCAM is mislocalized in glial cells. In order to investigate whether the relationship between Mlc1 and GlialCAM is species-specific, we first identified MLC-related genes in zebrafish and generated an mlc1(-/-) zebrafish. We have characterized mlc1(-/-) zebrafish both functionally and histologically and compared the phenotype with that of the Mlc1(-/-) mice. In mlc1(-/-) zebrafish, as in Mlc1(-/-) mice, Glialcam is mislocalized. Re-examination of a brain biopsy from an MLC patient indicates that GLIALCAM is also mislocalized in Bergmann glia in the cerebellum. In vitro, impaired localization of GlialCAM was observed in astrocyte cultures from Mlc1(-/-) mouse only in the presence of elevated potassium levels, which mimics neuronal activity. In summary, here we demonstrate an evolutionary conserved role for MLC1 in regulating glial surface levels of GLIALCAM, and this interrelationship explains why patients with mutations in either gene (MLC1 or GLIALCAM) share the same clinical phenotype.

DOI: https://doi.org/10.1093/hmg/ddu231

Human Molecular Genetics, 2014, Vol. 23, No. 19 **5069–5086**
doi:10.1093/hmg/ddu231
Advance Access published on May 12, 2014

Megalencephalic leukoencephalopathy with subcortical cysts protein 1 regulates glial surface localization of GLIALCAM from fish to humans

Sònia Sirisi[1,4,†], Mónica Folgueira[5,†], Tania López-Hernández[1], Laura Minieri[6], Carla Pérez-Rius[1], Héctor Gaitán-Peñas[1], Jingjing Zang[7], Albert Martínez[2], Xavier Capdevila-Nortes[1], Pedro De La Villa[8], Upasana Roy[9,10], A. Alia[9,10], Stephan Neuhauss[7], Stefano Ferroni[6], Virginia Nunes[3,4,11], Raúl Estévez[1,12,‡,*] and Alejandro Barrallo-Gimeno[1,12,‡,*]

[1]Sección de Fisiología, Departamento de Ciencias Fisiológicas II, [2]Department of Cell Biology and [3]Sección de Genética, Departamento de Ciencias Fisiológicas II, Universidad de Barcelona, Barcelona, Spain [4]Laboratorio de Genética Molecular-IDIBELL, L'Hospitalet de Llobregat, Spain [5]Department of Cell & Molecular Biology, University of A Coruña, A Coruña, Spain [6]Department of Pharmacy and Biotecnology, University of Bologna, Bologna, Italy [7]Institute of Molecular Life Sciences, University of Zurich, Zurich, Switzerland [8]Department of Systems Biology, University of Alcalá, Alcalá de Henares, Madrid, Spain [9]Leiden Institute of Chemistry, Leiden University, Leiden, The Netherlands [10]Institute of Medical Physics and Biophysics, University of Leipzig, Leipzig, Germany [11]U-730 and [12]U-750, Centro de Investigación en red de Enfermedades Raras (CIBERER), ISCIII, Barcelona, Spain

Received March 19, 2014; Revised and Accepted May 8, 2014

Megalencephalic leukoencephalopathy with subcortical cysts (MLC) is a leukodystrophy characterized by myelin vacuolization and caused by mutations in *MLC1* or *GLIALCAM*. Patients with recessive mutations in either *MLC1* or *GLIALCAM* show the same clinical phenotype. It has been shown that GLIALCAM is necessary for the correct targeting of MLC1 to the membrane at cell junctions, but its own localization was independent of MLC1 *in vitro*. However, recent studies in *Mlc1*$^{-/-}$ mice have shown that GlialCAM is mislocalized in glial cells. In order to investigate whether the relationship between Mlc1 and GlialCAM is species-specific, we first identified MLC-related genes in zebrafish and generated an *mlc1*$^{-/-}$ zebrafish. We have characterized *mlc1*$^{-/-}$ zebrafish both functionally and histologically and compared the phenotype with that of the *Mlc1*$^{-/-}$ mice. In *mlc1*$^{-/-}$ zebrafish, as in *Mlc1*$^{-/-}$ mice, Glialcam is mislocalized. Re-examination of a brain biopsy from an MLC patient indicates that GLIALCAM is also mislocalized in Bergmann glia in the cerebellum. *In vitro*, impaired localization of GlialCAM was observed in astrocyte cultures from *Mlc1*$^{-/-}$ mouse only in the presence of elevated potassium levels, which mimics neuronal activity. In summary, here we demonstrate an evolutionary conserved role for MLC1 in regulating glial surface levels of GLIALCAM, and this interrelationship explains why patients with mutations in either gene (*MLC1* or *GLIALCAM*) share the same clinical phenotype.

INTRODUCTION

Megalencephalic leukoencephalopathy with subcortical cysts (MLC) is a rare type of congenital leukodystrophy characterized mainly by myelin vacuolization and early onset of macrocephaly (1). Magnetic resonance imaging (MRI) of patient's brains shows diffuse signal abnormality, and this method is used for diagnosis during childhood (2). MLC is caused by mutations

*To whom correspondence should be addressed at: Facultat de Medicina, Departament de Ciències Fisiològiques II, Universitat de Barcelona, C/Feixa Llarga s/n 08907 L'Hospitalet de Llobregat, Barcelona, Spain. Tel: +34 934039781; Fax: +34 934024268; Email: restévez@ub.edu (R.E.); abarrallo@ub.edu (A.B.-G.)
†These authors contributed equally.
‡These authors share last authorship.

in either *MLC1* (MIM #605908) or *GLIALCAM* (MIM #611642) genes (3,4).

MLC1 encodes for a membrane protein, which is expressed in several brain barriers, mainly in ependymal cells, astrocytes surrounding blood vessels and Bergmann radial glia in the cerebellum. In all cells, MLC1 is localized at cell junctions (5–7). Surprisingly, MLC1 is not expressed in oligodendrocytes, the site of the primary pathology of MLC (8). Mutations have been found across the whole coding sequence (3,9–11), which cause protein folding defects that lead to degradation of MLC1 (12,13). The function of MLC1 is still unknown, although it has been related to the activation of volume-regulated anion currents (VRAC) (14,15), involved in cellular osmotic response. It has been indicated that a reduced VRAC activity may lead to intracellular water accumulation and to the vacuolization observed in patients (15,16). In addition, other studies have suggested that MLC1 cooperates with the Na^+/K^+-ATPase and the TRPV4 channel (17,18), although the exact mechanism is still unknown.

GlialCAM (also called HEPACAM due to its original discovery in hepatic cancer cells) is a cell adhesion molecule of the immunoglobulin family (19) that is mostly expressed in glial cells (20) and co-localizes with MLC1 at astrocyte–astrocyte junctions (4). MLC patients with recessive mutations in *GLIALCAM* (known as MLC2A type of MLC, MIM #613925) present the same phenotype as patients carrying recessive mutations in *MLC1* (MLC1 type of MLC, MIM #604004) (4,21). Some MLC patients have dominant mutations in the *GLIALCAM* gene (MLC2B type of MLC, MIM #613926), and these are associated to various degrees of phenotypic expression, ranging from a transient benign form of MLC, to macrocephaly and mental retardation with or without autism (4,21).

Both data obtained from *in vitro* and from *GlialCAM*$^{-/-}$ mice have demonstrated that GlialCAM is necessary for MLC1 to exit the endoplasmatic reticulum and target cell junctions (13,15,22). Furthermore, a mistargeting of both GlialCAM and MLC1 to cell junctions has been shown by *in vitro* studies with most missense *GLIALCAM* mutations (either recessive or dominant) and with *GlialCAM*$^{dn/dn}$ knock-in mice harbouring a dominant mutation (4,13,22,23). In contrast, GlialCAM seems to be able to traffic to cell junctions by itself (13,19). Thus, the overlapping phenotype of MLC1 and MLC2A patients can be understood because of the cardinal role of MLC1 in the pathogenesis of MLC.

However, GlialCAM, but not MLC1, is detected in oligodendrocytes (4,20); it was also found that GlialCAM functions as an auxiliary glial-specific subunit of the broadly expressed ClC-2 chloride channel (24). Furthermore, MLC-related *GLIALCAM* mutations impair the trafficking of ClC-2 to cell junctions (23,24). Analyses of *GlialCAM*$^{-/-}$ and *GlialCAM*$^{dn/dn}$ knock-in mice have shown that localization of ClC-2 in glial junctions is dependent on GlialCAM (22). Thus, based on these *in vitro* and *in vivo* data, patients carrying recessive *GLIALCAM* mutations should be more severely affected than patients carrying recessive *MLC1* mutations, as ClC-2 channel may also be affected in those carrying *GLIALCAM* mutations. However, there are no clinical differences between these two types of patients.

Recent studies with *Mlc1*$^{-/-}$ mice have shown that, contrary to what was expected based on the lack of direct interaction between MLC1 and ClC-2, GlialCAM and ClC-2 are mislocalized in astrocytes and oligodendrocytes when MLC1 is absent (22). Based on cell culture data, it was indicated that MLC1 and ClC-2 could indirectly interact through homotypic extracellular GlialCAM-mediated interactions (22), as previously suggested (25). These results indicate that lack of function of ClC-2 may be involved in the pathogenesis of MLC (22). Lack of ClC-2 function has also been associated with a distinct form of leukoencephalopathy (26).

The mislocalization of GlialCAM found in *Mlc1*$^{-/-}$ mice contradicts previous results obtained using RNA interference of *Mlc1* in rat astrocytes and localization studies of GLIALCAM around blood vessels in a sample from an MLC1 patient (13). Although RNA interference may not completely reproduce the gene knockout phenotype, we have previously shown that Mlc1 RNAi induces a significant decrease in Mlc1 protein levels (12,13). Thus, it is unclear if GlialCAM is unstable without MLC1 only in mice, or whether this is a general mechanism.

To solve this controversy, we decided to examine the relationship between Mlc1 and GlialCAM in other animal species. We generated a zebrafish model for MLC based on the lack of mlc1. As in mice, characterization of the zebrafish model revealed that loss of mlc1 impairs the correct localization of glialcam. Re-examination of the brain biopsy from a MLC1 patient that had been previously studied revealed that GlialCAM was mislocalized in Bergmann glia. These results confirm that the MLC1-dependent localization of GlialCAM is a general mechanism, as data from *Mlc1*$^{-/-}$ mouse had shown. As in the RNA interference experiments, cultured astrocytes from *Mlc1*$^{-/-}$ mice show normal GlialCAM localization, but slightly reduced VRAC activity. However, we observed that mimicking neuronal activity in *Mlc1*$^{-/-}$ astrocyte cultures causes GlialCAM mislocalization. Hence, data presented here explain previous discrepancies and reveal a conserved activity-regulated role of MLC1 in determining the localization of GLIALCAM.

RESULTS

GlialCAM is also mislocalized in Mlc1$^{-/-}$ astrocytes close to ependymal cells

In situ hybridization and immunohistochemistry studies have demonstrated that MLC1 and GLIALCAM co-localize in astrocytes close to brain barriers, Bergmann glia and ependymal cells, and that GLIALCAM is additionally expressed in oligodendrocytes (4,6,7,20). In *Mlc1*$^{-/-}$ mice, GlialCAM is mislocalized in astrocytes, Bergmann glia and oligodendrocytes (22). We examined whether GlialCAM was also mislocalized in ependymal cells by means of electron microscopy. To our surprise, gold particle-labelled antibodies showed that Mlc1 is not present in ependymal cells, but rather in astrocyte–astrocyte contacts below ependymal cells (Fig. 1A and C). Control experiments in *Mlc1*$^{-/-}$ mice confirmed the specificity of the signal (Fig. 1B and D). GlialCAM co-localized with Mlc1 in subependymal astrocyte–astrocyte contacts (Fig. 1E and G), and, as observed previously in astrocytes and oligodendrocytes, GlialCAM was also mislocalized in astrocytes near ependymal cells in *Mlc1*$^{-/-}$ mice (Fig. 1F and H). Thus, we conclude that the absence of *Mlc1* in mice causes mistargeting of GlialCAM in all types of glial cells.

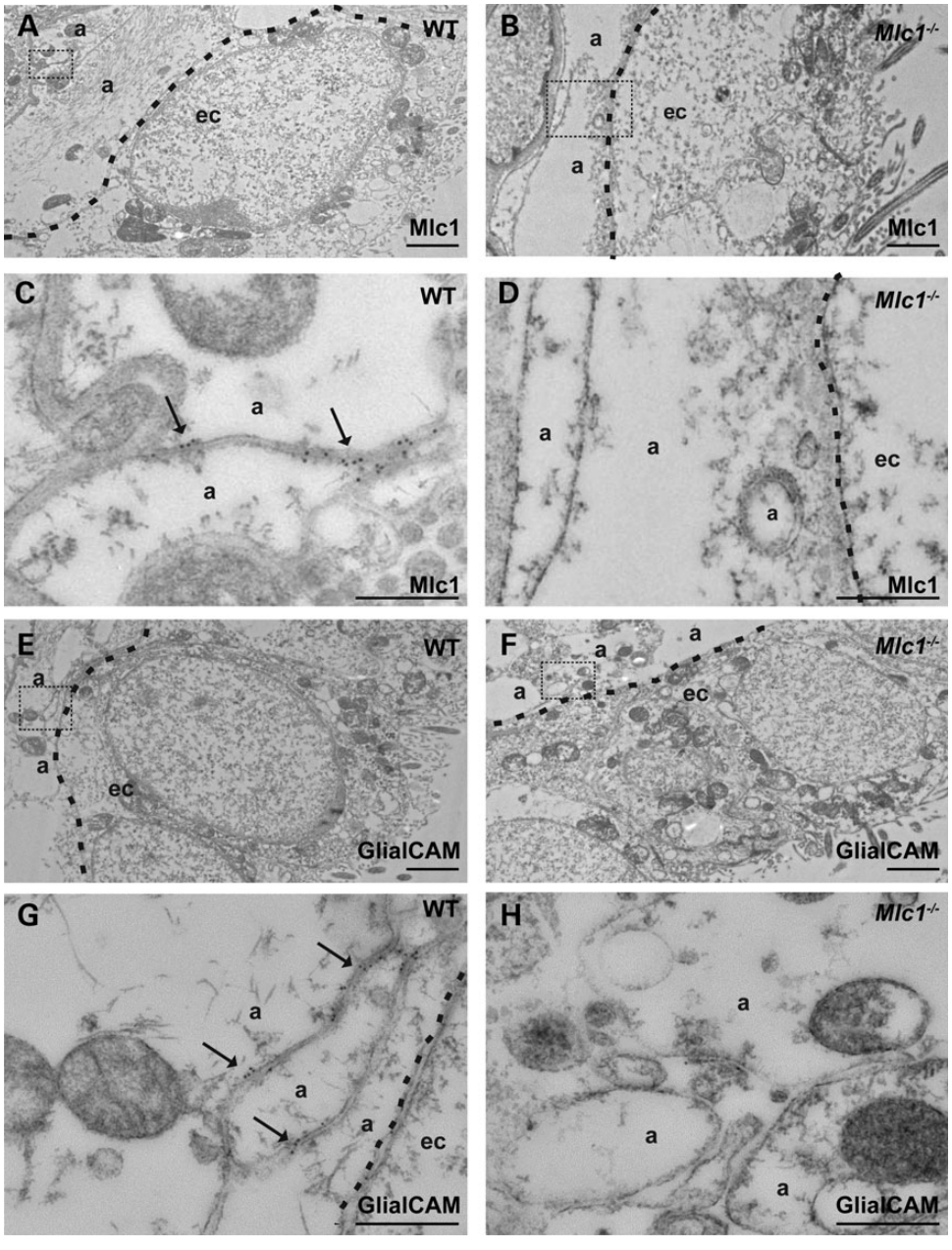

Figure 1. GlialCAM does not localize to astrocyte junctions in subependymal astrocytes in *Mlc1*$^{-/-}$ mice. (**A**–**D**) EM immunolabelling of ependymal cells shows localization of Mlc1 in astrocyte–astrocyte junctions (arrows) near ependymal cells (A and C). Dotted lines highlight boundaries between ependymal cells (ec) and inner astrocytic processes (a). The signal was specific as it was absent in Mlc1$^{-/-}$ mice (B and D). The insets in (A) and (B) are shown amplified in (C) and (D). Scale bars: (A, B): 2 μm; (C, D): 500 nm. (**E**–**H**) EM immunolabelling images of GlialCAM in astrocyte junctions below ependymal cells (arrows) (E, G). GlialCAM protein could not be observed in astrocyte–astrocyte junctions in *Mlc1*$^{-/-}$ mice (F, H). The insets in (E) and (F) are shown amplified in (G) and (H). Scale bars: (E and F): 2 μm; (G and H): 500 nm.

Identification of MLC-related genes in zebrafish

To address whether this Mlc1-dependent mislocalization of GlialCAM was a conserved feature, we decided to generate an *Mlc1*-deficient animal model in another species. By means of sequence database inspection, we found that genes encoding the orthologue of human *MLC1* are present in all vertebrates, including zebrafish (*Danio rerio*), that has a single orthologue (Supplementary Material, Fig. S1A). In contrast, metazoan model organisms, such as *Drosophila melanogaster* and *Caenorhabditis elegans*, which lack myelin, do not possess *MLC1* orthologues (3). For *GLIALCAM*, we observed that the teleost-specific genome duplication yielded two *glialcam* paralogues: *glialcama* and *glialcamb* (Supplementary Material, Fig. S2A).

Sequence comparison between zebrafish *mlc1* and its human ortholog showed an overall 53% identity that was higher (63%) at the putative transmembrane domains and the terminal part of the C-terminus (Supplementary Material, Fig. S1B). Both *glialcam* paralogues showed a 76% identity with human

GLIALCAM across the two extracellular Ig-domains and the putative transmembrane domain, but the conservation of the C-terminal intracellular domain was very low, saved for a stretch of residues in the central part (Supplementary Material, Fig. S2B).

We cloned zebrafish *mlc1* and both *glialcam* paralogues, fused to an intracellular FLAG tag, and expressed them transiently in HeLa cells. Importantly, glialcama could be predominantly detected in cell junctions (Fig. 2A), while glialcamb was found in a diffuse manner (Fig. 2B). Like its human counterpart (13), glialcama was able to target zebrafish mlc1 (Fig. 2C–E) and rat chloride channel ClC-2 (24) (Fig. 2F–H) to cell junctions. Furthermore, glialcama and not glialcamb was able to modify the functional properties of rat ClC-2-mediated currents in *Xenopus* oocytes. Glialcama, as with the human ortholog (24), not only increased ClC-2-mediated currents, but also changed rectification and activation properties (Fig. 2I–L). To additionally verify that glialcama behaves as human GLIALCAM, we analysed glialcama variants containing MLC-related mutations in conserved residues (Supplementary Material, Fig. S2B) that have previously shown trafficking defects (13). As happened in human *GLIALCAM* (4), we observed that the introduction of MLC-related mutations in glialcama negatively affected its junctional localization without substantially interfering with its expression levels (Supplementary Material, Fig. S3A–C).

These results suggest that zebrafish glialcama, and not glialcamb, could perform the same physiological functions as human GLIALCAM. Therefore, we decided to focus our studies on this zebrafish paralogue.

Generation of a mutant mlc1 zebrafish line

We generated a zebrafish *mlc1* knockout line by sequencing the first exons of the *mlc1* gene on the ENU-based TILLING library at the laboratory of Dr C. Moens at the FHCRC (Seattle, USA). Unfortunately, we did not detect any stop, frameshift or splice site mutations that would potentially abolish normal protein expression. However, we detected a missense mutation (c.241T>G) in one allele (*mlc1*^{fh328}), resulting in the substitution of a conserved hydrophobic residue (isoleucine) for a charged one (arginine; p.81I>R) on the predicted first transmembrane domain of the protein. We hypothesized that the introduction of a positive charge in the transmembrane domain could be deleterious for its protein expression. In order to test this, we introduced the equivalent mutation (V64R, Supplementary Material, Fig. S1B) in human MLC1 carrying *HA* epitope tags (one at the *N*-terminus and the other extracellular) and assayed surface expression by an ELISA-based luminescence assay in *Xenopus* oocytes (Fig. 3A). We used oocytes because their incubation temperature (18°C) would reveal whether the mutation causes folding defects (27). No surface expression could be detected, confirming our hypothesis that the mutation was deleterious.

Therefore, the heterozygous founder zebrafish were pair-wise mated and out-crossed for several generations to eliminate any other background mutations from the original ENU mutagenesis (see Materials and Methods). As the mutation results in a novel *Dde*I restriction site, it was possible to perform RFLP genotyping, and gene sequencing confirmed the presence of the mutation (Fig. 3B and C). As our previous antibodies against human or mouse Mlc1 proteins did not recognize the zebrafish orthologue (data not shown), we developed a new rabbit polyclonal antibody that was able to detect zebrafish mlc1 (Fig. 3D and E). We assayed mlc1 expression in brain extracts from wild-type, heterozygous and homozygous *mlc1*^{fh328} adult fish siblings. No mlc1 protein expression could be detected in homozygotes, validating the allele *mlc1*^{fh328} as an *mlc1* knockout line, which we will refer to as *mlc1*$^{-/-}$ zebrafish from now on (Fig. 3F). As with the *Mlc1*$^{-/-}$ mouse (22), the homozygous *mlc1*$^{-/-}$ zebrafish turned out to be viable and fertile, with the expected mendelian ratio among adult descendants.

Expression pattern of mlc1 in the adult zebrafish brain and retina

We determined the expression pattern of *mlc1* in adult tissues by RT-qPCR (Fig. 4A) and western blot (Fig. 4B). This showed that *mlc1* is mainly expressed in the brain and at reduced levels in the eye. We performed immunofluorescence experiments to determine which cell types express mlc1 in the adult brain, using the *mlc1*$^{-/-}$ zebrafish as a control. Prominent immunoreactivity was observed at the ventricular and pial surface of the brain, and around some blood vessels (Fig. 4C, D, F). Additionally, mlc1 immunoreactivity was observed in radial processes within the brain parenchyma (Fig. 4D). Lack of staining in the *mlc1*$^{-/-}$ zebrafish brain confirmed the specificity of our results (Fig. 4E). Staining of mlc1 in the transgenic line *fli1a:GFP*, which expresses GFP in the vascular endothelium (28), confirmed that the mlc1 protein is present at astrocytic perivascular processes (Fig. 4F). mlc1 staining around brain ventricles and radial-like structures was also positive for glial fibrillary acid protein (gfap) antibody (Fig. 4G and H), indicating that these are astroglial-like cells (29). Thus, expression of mlc1 in the zebrafish brain is very similar to that found in humans.

We also analysed the localization of mlc1 in the retina. High expression of mlc1 was detected at the inner limiting membrane of the retina. Specificity of the antibody was confirmed by lack of staining in *mlc1*$^{-/-}$ zebrafish retina (Fig. 4I and J). Double immunostaining with gfap demonstrated that mlc1 was strongly expressed in Müller glia end-feet in the inner limiting membrane (Fig. 4K). Furthermore, we also observed weak mlc1 and gfap co-expression at fine radial glial processes away from the vitreal surface of the retina (Fig. 4K).

Glialcama localization in the adult brain and retina is affected in mlc1$^{-/-}$ zebrafish

As with *mlc1*, we determined the pattern of expression of *glialcama* using RT-qPCR in adult tissues. mRNA for *glialcama* was more broadly expressed compared with *mlc1*, but showed the highest expression levels in the brain. Detection of glialcama protein in tissue extracts by western blot using a newly developed glialcama antibody (Supplementary Material, Fig. S3D) confirmed its higher expression in the brain (Fig. 5B), and its presence in the eye.

We next addressed the localization of glialcama in brain and retina from wild-type and *mlc1*$^{-/-}$ zebrafish (Fig. 5C and D). Similar to mlc1, we detected strong immunoreactivity to glialcama in radial glial cell bodies and their processes (Fig. 5C and D), which were also positive for gfap (Fig. 5E). In contrast,

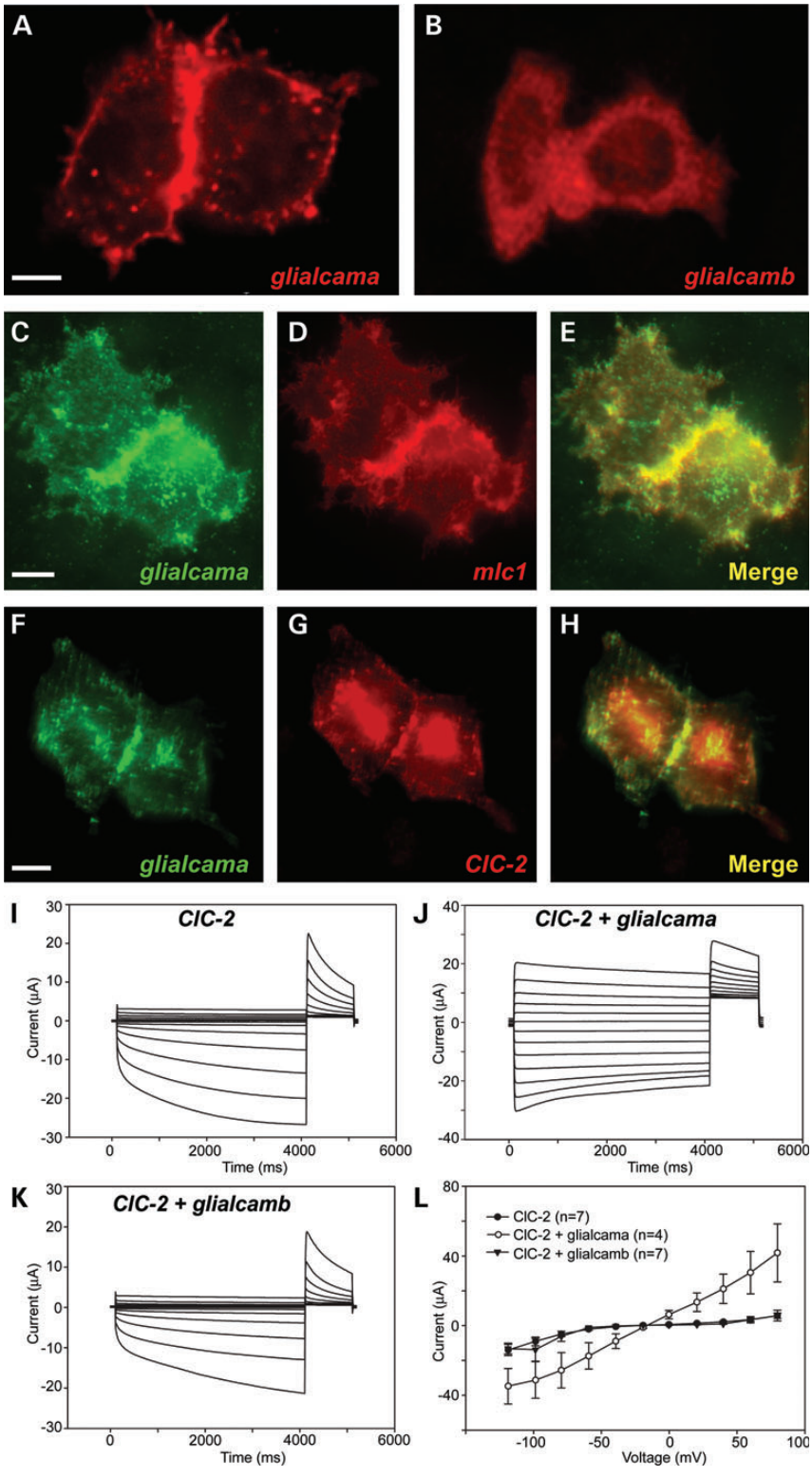

Figure 2. Characterization of the zebrafish orthologues of *Mlc1* and *Glialcam.* (**A** and **B**) *glialcama* and *glialcamb* were transfected separately in HeLa cells and detected through the FLAG epitope with immunofluorescence. While glialcama is specifically located in cell–cell junctions, glialcamb protein presented a diffuse location. Scale bar: 10 μm. (**C**–**E**) Co-transfection of *glialcama* and *mlc1* in HeLa cells reveals their co-localization at cell junctions. Scale bar: 10 μm. (**F**–**H**) Co-transfection of *glialcama* and rat *ClC-2* in HeLa cells reveals their co-localization at cell junctions. Scale bar: 10 μm. (**I**–**L**) A typical current trace mediated by rat ClC2 (I) expressed in oocytes and after co-expression with glialcama (J) or glialcamb (K). Only glialcama is able to modify the functional properties of ClC-2. The apparent inactivation observed sometimes at very negative voltages is an artefact caused by chloride depletion inside the oocytes (J). (L) Average steady-state current–voltage relationship of ClC-2 (black circles) and ClC-2 co-expressed with glialcama (white circles) or with glialcamb (triangles). Glialcama increased ClC-2-mediated conductance and changed its rectification properties.

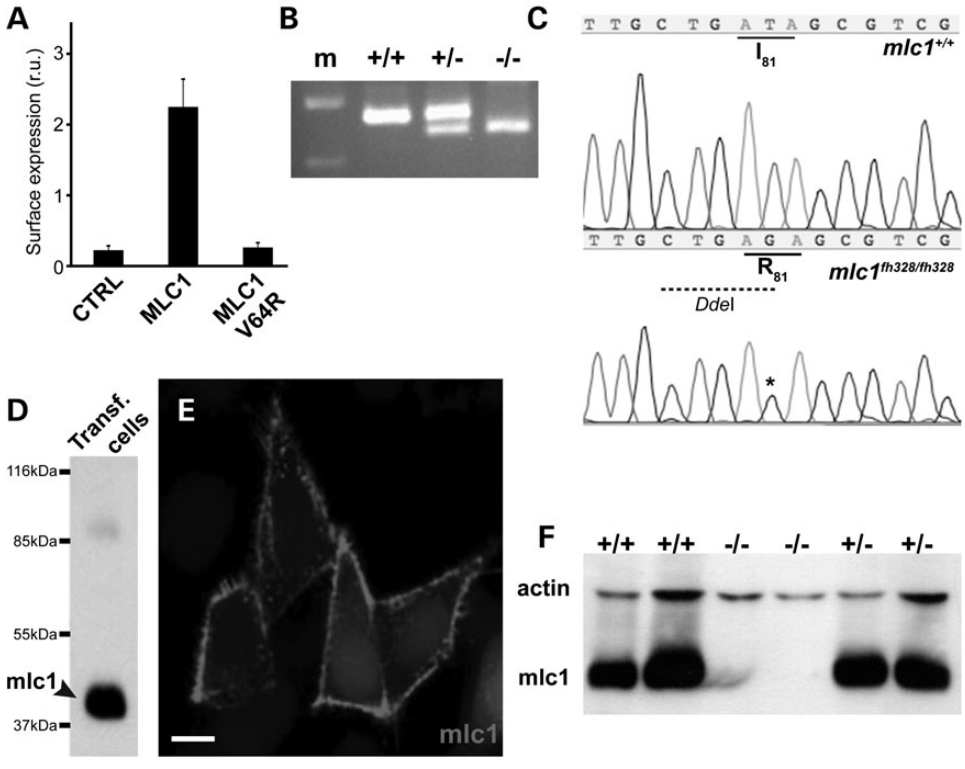

Figure 3. Generation of a zebrafish model for MLC based on the inactivation of mlc1. (**A**) Expression in *Xenopus* oocytes of human MLC1 carrying the V64R mutation abolishes its surface expression, as assayed by detection by an ELISA-based assay. (**B**) Restriction analysis with *Dde*I allows for the identification of wild-type (+/+), heterozygous (+/−) or homozygous mutant (−/−) fish of the *mlc1*^{fh328} allele. m: molecular weight marker. (**C**) Zebrafish *mlc1*^{fh328} allele originates the I81R mutation, and generates a *Dde*I restriction site. (**D** and **E**) Custom-generated antibody against mlc1 detects a protein of the expected molecular weight (around 42 kDa, arrowhead) and its localization in the membrane on *mlc1*-transfected HeLa cells. The band observed at about 85 kDa corresponds to mlc1 dimers. Scale bar (E): 10 μm. (**F**) Western blot of brain extracts from adult wild-type (+/+), heterozygous (+/−) or homozygous mutant (−/−) fish for the *mlc1*^{fh328} allele demonstrates the absence of the mlc1 protein in the homozygous zebrafish.

a more diffuse glialcama staining was observed in the same brain regions in *mlc1*$^{-/-}$ zebrafish (Fig. 5F). We addressed if lack of detection was due to reduced protein expression by western blot using brain extracts, but no changes in protein expression levels were observed (Fig. 5G). We also studied glialcama localization in the retina, as its laminar arrangement could allow easier visualization of subcellular mislocalization. As observed for mlc1, glialcama was highly expressed at Müller glia end-feet at the inner limiting membrane (Fig. 5H and I). This expression was absent in *mlc1*$^{-/-}$ zebrafish. Thus, as we observed in the brain, glialcama was mislocalized in the retina of *mlc1*$^{-/-}$ zebrafish (Fig. 5J).

We can conclude that lack of mlc1 in zebrafish causes glialcama mislocalization in glial cells in the brain and retina, in a similar manner to that found in *Mlc1*$^{-/-}$ mice (22).

Comparison of mouse and zebrafish Mlc1 knockout phenotypes

The phenotypes of Mlc1 mouse and zebrafish knockouts were compared. Histopathology of brain sections from *Mlc1*$^{-/-}$ mice revealed largely restricted myelin vacuolization in fibre tracts of the cerebellum (22). In agreement with these histology results, T_2-weighted MRI of the brain of *Mlc1*$^{-/-}$ mice showed lesions in white matter tracts of the cerebellum from about 6 months of age that increased with age (Fig. 6A and B). Measurement of brain volume revealed that the whole brain is bigger in *Mlc1*$^{-/-}$ than in wild-type mice at the same age (Fig. 6G).

In zebrafish, we analysed the brain of four adult (14 months old) *mlc1*$^{-/-}$ zebrafish by MRI. We only observed very minor lesions in the telencephalon and mesencephalon (Fig. 6C–F) which showed similar relaxation times as cerebrospinal fluid, thus suggesting that they were due to increased fluid. As in mice, measurements of different brain areas revealed that the telencephalon seems larger in comparison with the whole brain in mutant than in wild-type zebrafish (Fig. 6H).

Thus, both animal models showed two typical MLC features: megalencephaly and increased fluid accumulation. However, we failed to observe the presence of vacuoles in any region of the zebrafish brain by general histological procedures (eight different animals; Supplementary Material, Fig. S4A and B) or electron transmission microscopy (four different animals; Supplementary Material, Fig. S4E and F). We conclude that the *mlc1*$^{-/-}$ zebrafish develops less severe lesions than the *Mlc1*$^{-/-}$ mice in the brain, which in turn also develops a less severe phenotype than humans.

As glialcama and mlc1 are co-expressed in Müller cells in the retina, we also studied and compared retina morphology between mice and zebrafish. As in *Mlc1*$^{-/-}$ mice (22), the retina of *mlc1*$^{-/-}$ zebrafish did not show lesions after histological staining (Supplementary Material, Fig. S4C and D). We also

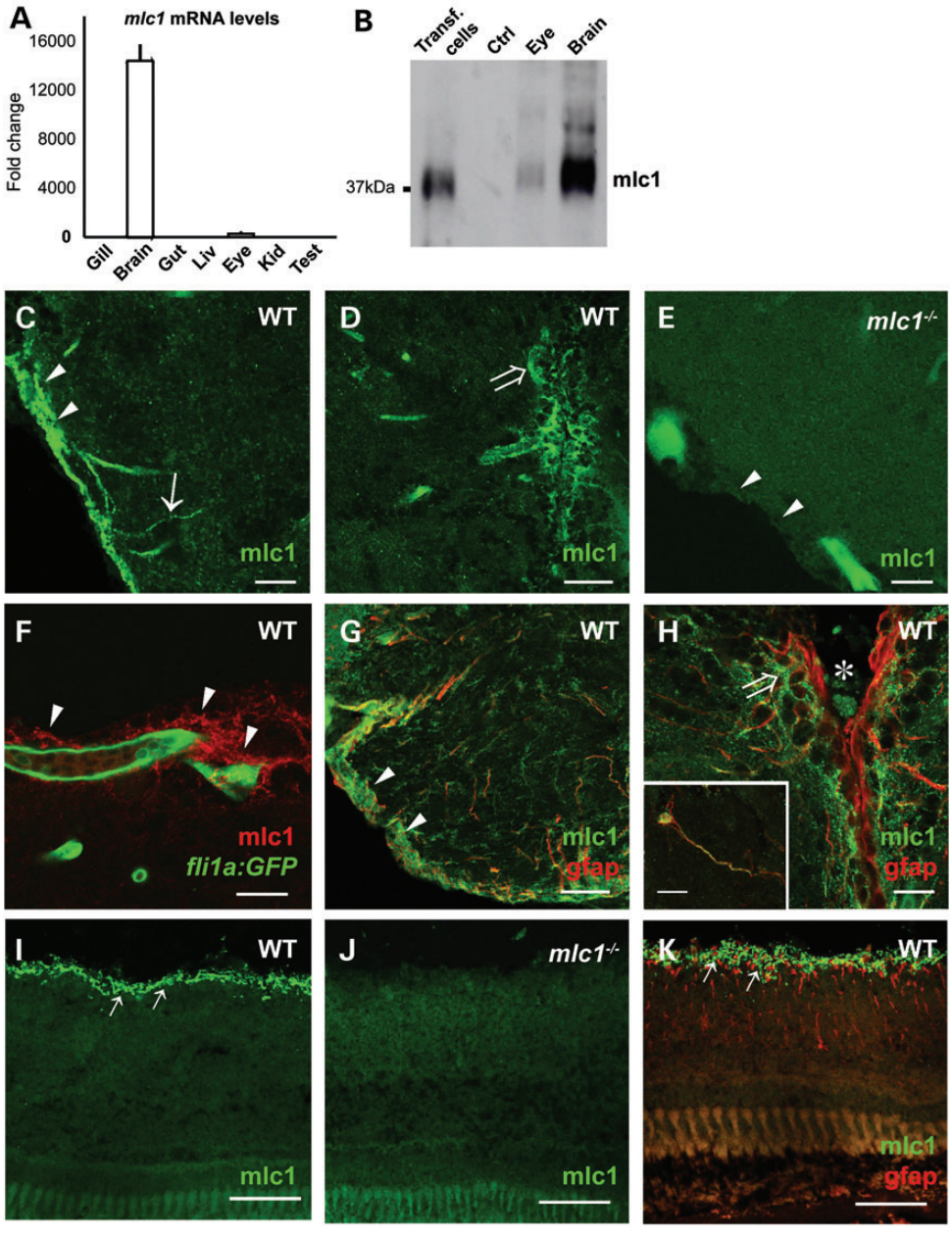

Figure 4. *mlc1* expression and localization pattern in adult zebrafish. (**A**) qPCR with RNA from adult tissues shows the expression of *mlc1* almost exclusively in the brain, and at a lesser level in the eye. (**B**) Western blot with the custom mlc1 antibody shows its expression on the brain and eye. As controls, we used extracts from mlc1-transfected and untransfected HeLa cells. (**C**–**F**) Immunofluorescence detection of mlc1 in the zebrafish adult brain. (C) mlc1 is expressed in radial glia processes (arrow) and pial end-feet (arrowheads). (D) mlc1 expression surrounds the ventricle of the brain (open arrow). (E) No immunoreactivity is observed in *mlc1*$^{-/-}$. Arrowheads point to the pial surface of the brain. Scale bars: 20 μm. (F) Localization of mlc1 (red) in glial perivascular processes (arrowheads) around blood vessels (green) in the brain of a *fli1a::GFP* transgenic zebrafish. Scale bar: 10 μm. (**G** and **H**) mlc1 co-localizes with the astrocytic protein gfap in the zebrafish adult brain at the pial (arrowhead in G) and ventricular surfaces of the brain (open arrow in H). Asterisk labels the ventricle. Scale bars: 15 μm. Inset: gfap and mlc1 co-expression at the cell body and radial processes of an astrocyte located in a subependymal zone. Scale bar: 15 μm. (**I**–**K**) Localization of mlc1 on the retina. (I) mlc1 is expressed in the inner limiting membrane (arrows) of the retina. (J) No immunoreactivity against mlc1 is observed in *mlc1*$^{-/-}$ zebrafish retina. (K) Double immunofluorescence with gfap (red) confirms mlc1 expression (green) in radial glia processes and Müller glia end-feet (arrow) at inner limiting membrane. Scale bars: 100 μm.

evaluated the visual function by recording electro-retinograms (ERG) in *Mlc1*$^{-/-}$ mice and *mlc1*$^{-/-}$ zebrafish (Supplementary Material, Fig. S5). No significant differences of the means of b-wave amplitude between wild-type and *mlc1*$^{-/-}$ fish at any light condition were observed (Supplementary Material, Fig. S5A). The relation of normalized b-wave amplitude and the light intensity (inset in Supplementary Material, Fig. S5A) showed complete overlaps between the two groups, suggesting that the sensitivity in *mlc1*$^{-/-}$ fish does not differ from wild-types. Similar observations have been found in 2-month-old adults (Supplementary Material, Fig. S5B). Similar tests were performed on 1-year-old adult *Mlc1*$^{-/-}$ mice. Analysis of the

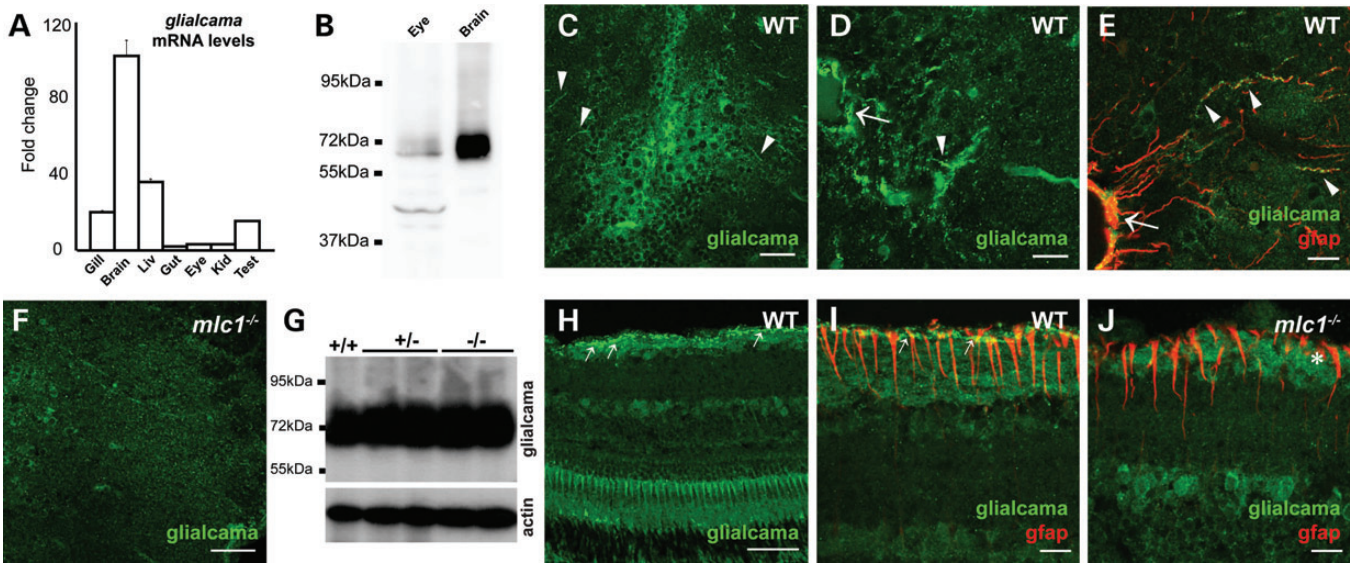

Figure 5. Glialcama is mislocalized in *mlc1*$^{-/-}$ zebrafish. (**A**) qPCR with RNA from adult tissues shows the highest expression of *glialcama* in the brain, but also in other tissues. (**B**) Western blot with the custom antibody shows glialcama expression on the brain and eye. (**C** and **D**) Immunofluorescence detection of glialcama in the zebrafish adult brain. We observed glialcam expression both in radial processes (arrowheads in C and D) and end-feet (arrow in D). Scale bars: 50 μm in (C), 20 μm in (D). (**E**) Co-localization of glialcama (green) and the astrocytic protein gfap (red) at radial glia processes (arrowheads) and end-feet (arrow). Scale bar: 20 μm. (**F**) glialcama signal is more diffuse in the brain of *mlc1*$^{-/-}$ zebrafish. Scale bar: 50 μm. (**G**) Expression levels of glialcama in the brain are not different between wild-type (+/+), heterozygous (+/−) and *mlc1*$^{-/-}$ zebrafish. Actin level was used as a loading control. (**H**–**J**) Localization of glialcama on the retina. (H) Strong expression is observed at the inner limiting membrane (arrows) of the retina in wild-type zebrafish. (**I**) Double immunofluorescence with gfap confirms glialcama expression in Müller glia end-feet (arrows). Note the funnel-like form of Müller glia end-feet. (J) In *mlc1*$^{-/-}$ zebrafish, only a diffuse labelling is observed with no strong expression in the inner limiting membrane (asterisk). Scale bars: 100 μm in (H), 20 μm in (I) and (J).

amplitudes of the different components of the ERG showed no significant differences between wild-type and *Mlc1*$^{-/-}$ mice (Supplementary Material, Fig. S5C).

Human GLIALCAM is also mislocalized in the Bergmann glia of a MLC1 patient

Our studies with *Mlc1*$^{-/-}$ mice and *mlc1*$^{-/-}$ zebrafish have revealed mislocalization of GlialCAM in astrocytes and oligodendrocytes. However, previous studies from a biopsy of a MLC patient indicated that GLIALCAM was not mislocalized around blood vessels in the cortex (13).

We re-examined the localization of GLIALCAM in the cerebellum of this same human brain biopsy. We focused on the cerebellum, as it is more severely affected in *Mlc1*$^{-/-}$ mice (22). As previously shown (13), we could not detect MLC1 in Bergmann glia from the MLC patient (Fig. 7A–F). In addition, staining with GLIALCAM antibodies revealed that it was in fact mislocalized in Bergmann glia in the MLC patient (Fig. 7G–L). Control staining with GFAP revealed that these changes were not due to defects in the integrity of the tissue. Thus, we can conclude that the mislocalization of GLIALCAM caused by the absence of MLC1 is a conserved feature from fish to humans, even though the phenotype is more severe as we climb the evolutionary ladder.

VRAC activity in cultured astrocytes from Mlc1$^{-/-}$ mice is still present

We cultured astrocytes from *Mlc1*$^{-/-}$ mice and analysed GlialCAM localization. Unexpectedly, lack of Mlc1 did not change GlialCAM localization (Fig. 8A–D) and expression (Fig. 8E) in *Mlc1*$^{-/-}$ astrocyte cultures. This result agreed with previous experiments that showed that knocking down Mlc1 in rat astrocytes changed neither the expression nor the localization of GlialCAM in cell junctions (13).

As MLC1 have been related with the activity of VRAC (14,15), we analysed chloride currents in Mlc1$^{-/-}$ astrocyte cultures. In wild-type and *Mlc1*$^{-/-}$ astrocytes, replacing intra- and extracellular Na^+ and K^+ ions with Cs^+ (to block sodium and potassium currents) and with symmetric Cl^-, the whole-cell background conductance was very low (Fig. 8F). In both type of astrocytes, hypotonicity challenge promoted a large, reversible increase in ramp current in the whole range of membrane potentials (Fig. 8F and Supplementary Material, Fig. S6A and C). These hypotonicity-activated currents reversed at ∼0 mV, were blocked by the specific VRAC inhibitor 4-(2-butyl-6,7-dichlor-2-cyclopentylindan-1-on-5-yl) oxobutyric acid (DCPIB) (30), and showed instantaneous activation and time-dependent inactivation at more positive potentials (Fig. 8F and Supplementary Material, Fig. S6A–D). These data indicated that hypotonicity-activated VRAC channels in wild-type and *Mlc1*$^{-/-}$ mouse astrocytes which are functionally identical to those described in rat astrocytes (31,32). The observation that the putative ClC-2 inhibitor cadmium (33) did not affect the hypotonicity-activated currents (Supplementary Material, Fig. S6E and F) strongly indicated that these Cl^- currents were not mediated by ClC-2, which is also present in mouse astrocytes (34). Comparison of VRAC amplitudes between wild-type and *Mlc1*$^{-/-}$ astrocytes indicated that VRAC was slightly reduced in astrocytes obtained from *Mlc1*$^{-/-}$ mouse (Fig. 8G). These results support the view that Mlc1 does not mediate directly

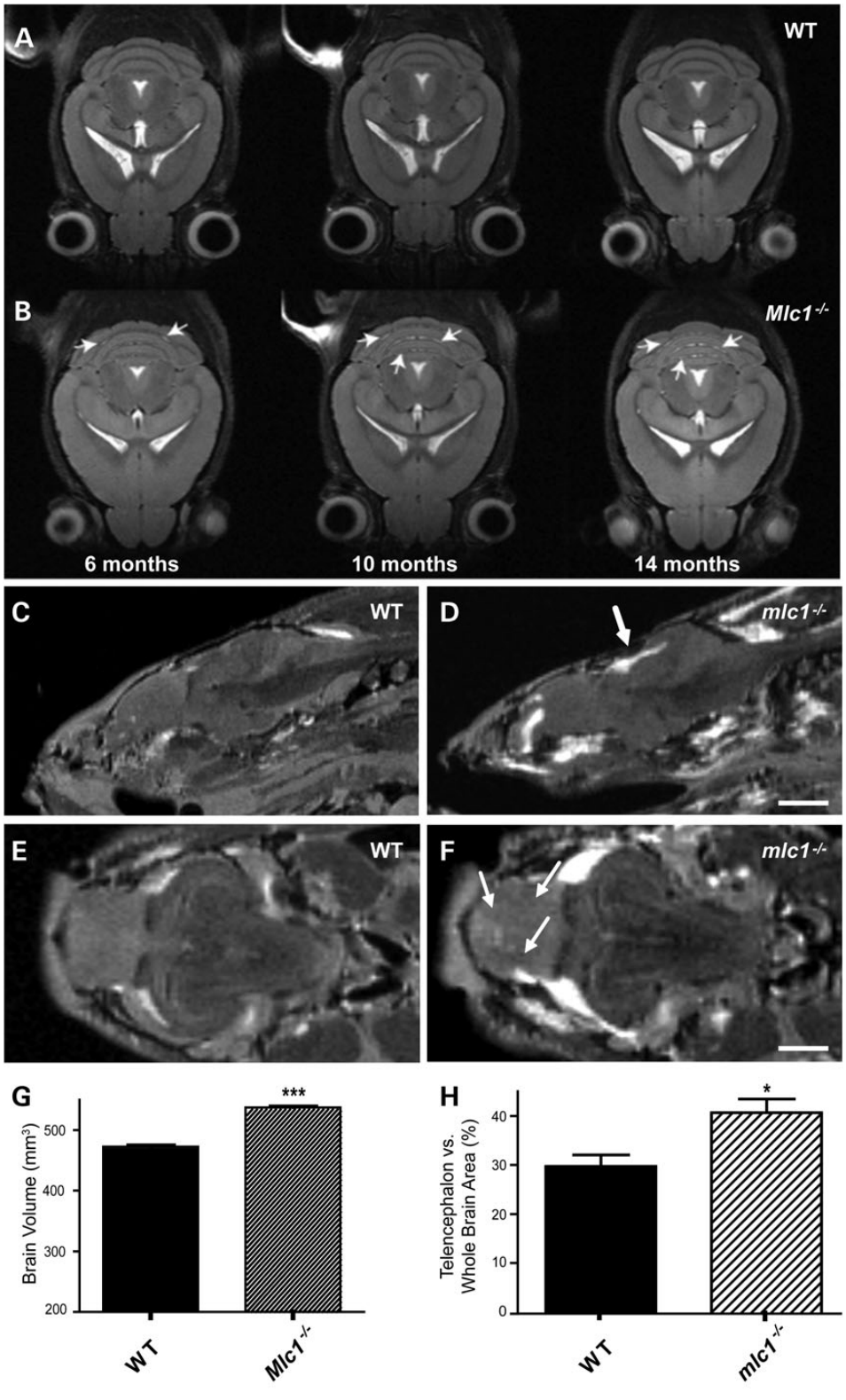

Figure 6. MRI of *Mlc1*$^{-/-}$ mice and *mlc1*$^{-/-}$ zebrafish. (**A** and **B**) MRI of mice from different ages show progressive presence of white matter lesions (arrows) in the cerebellum of *Mlc1*$^{-/-}$ animals (B), but not in wild-type mice (A). (**C**–**F**) MRI of adult zebrafish reveals the presence of small lesions in the mesencephalon (thick arrow in D) and telencephalon (arrows in F) in *mlc1*$^{-/-}$ zebrafish. Hyperintense signals in (D) and (F) may correspond to fat containing tissue in or around the brain. (C) and (E) correspond to images from wild-type zebrafish. Scale bars: 1 mm in (C) and (D), 500 μm in (E) and (F). (**G**) Brain volume is higher in *Mlc1*$^{-/-}$ mice. Brain volume was estimated by quantifying the area of consecutive MRI images using ImageJ. Data correspond to seven wild-type and seven *Mlc1*$^{-/-}$ mice ($P < 0.0001$). (**H**) Telencephalon appears bigger relative to the whole brain in *mlc1*$^{-/-}$ zebrafish ($P < 0.05$).

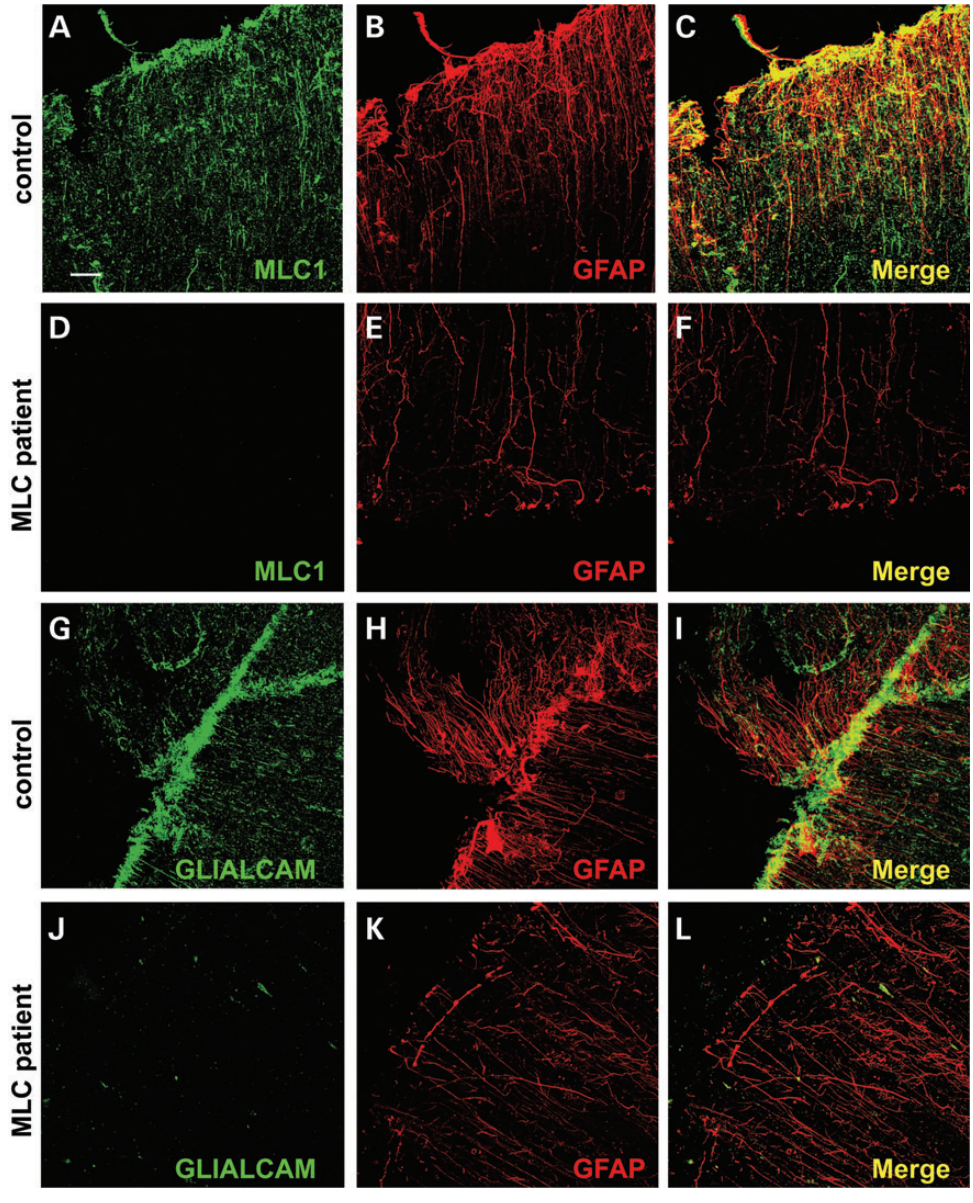

Figure 7. GLIALCAM is mislocalized in the cerebellum of a patient with a missense mutation in *MLC1*. (**A**–**F**) Immunofluorescence detection of MLC1 and GFAP proteins in the cerebellum of a control subject (A–C) and an MLC patient (D-F) carrying a homozygous mutation in *MLC1* shows the absence of the MLC1 protein in the patient. Scale bar: 40 μm. (**G**–**L**) Immunofluorescence detection of GLIALCAM and GFAP proteins in the cerebellum of a control subject (G–I) and an MLC patient (J–L) carrying a homozygous mutation in *MLC1* shows the diffuse signal for GLIALCAM in the absence of MLC1.

VRAC current. To detect whether the non-statistically significant VRAC reduction may lead to astrocyte vacuolation, we stained wild-type (Fig. 8H) and *Mlc1*$^{-/-}$ astrocytes (Fig. 8I) with the freely diffusible fluorescent reagent calcein. Vacuoles were more frequently observed in *Mlc1*$^{-/-}$ astrocytes (Fig. 8J).

Glialcam localization is dependent on Mlc1 with high extracellular potassium concentration

Why is GlialCAM mislocalized in *Mlc1*$^{-/-}$ astrocytes in tissue and not in culture? Mislocalization of GlialCAM in humans was better observed in Bergmann glia, which are bathed in a high extracellular potassium concentration due to cerebellar neuronal activity (35). Thus, we treated cultured astrocytes obtained from wild-type and *Mlc1*$^{-/-}$ mice with physiological medium or with an isosmotic solution with higher potassium concentration, mimicking neuronal activity. In wild-type astrocytes under high potassium concentration, there was no change on the localization of Mlc1 (Fig. 9A–D), but there was a slight increase of GlialCAM in cell junctions. When similar experiments were repeated in astrocytes from *Mlc1*$^{-/-}$, GlialCAM was detected intracellularly after high-potassium treatment (Fig. 9E–H). This effect was even more evident when astrocytes were infected with adenoviruses expressing human Flag-tagged GLIALCAM (Fig. 9I–L). Control staining with the junctional marker β-catenin revealed that these distribution changes caused by increasing extracellular potassium were specific to GlialCAM (Fig. 9M–P).

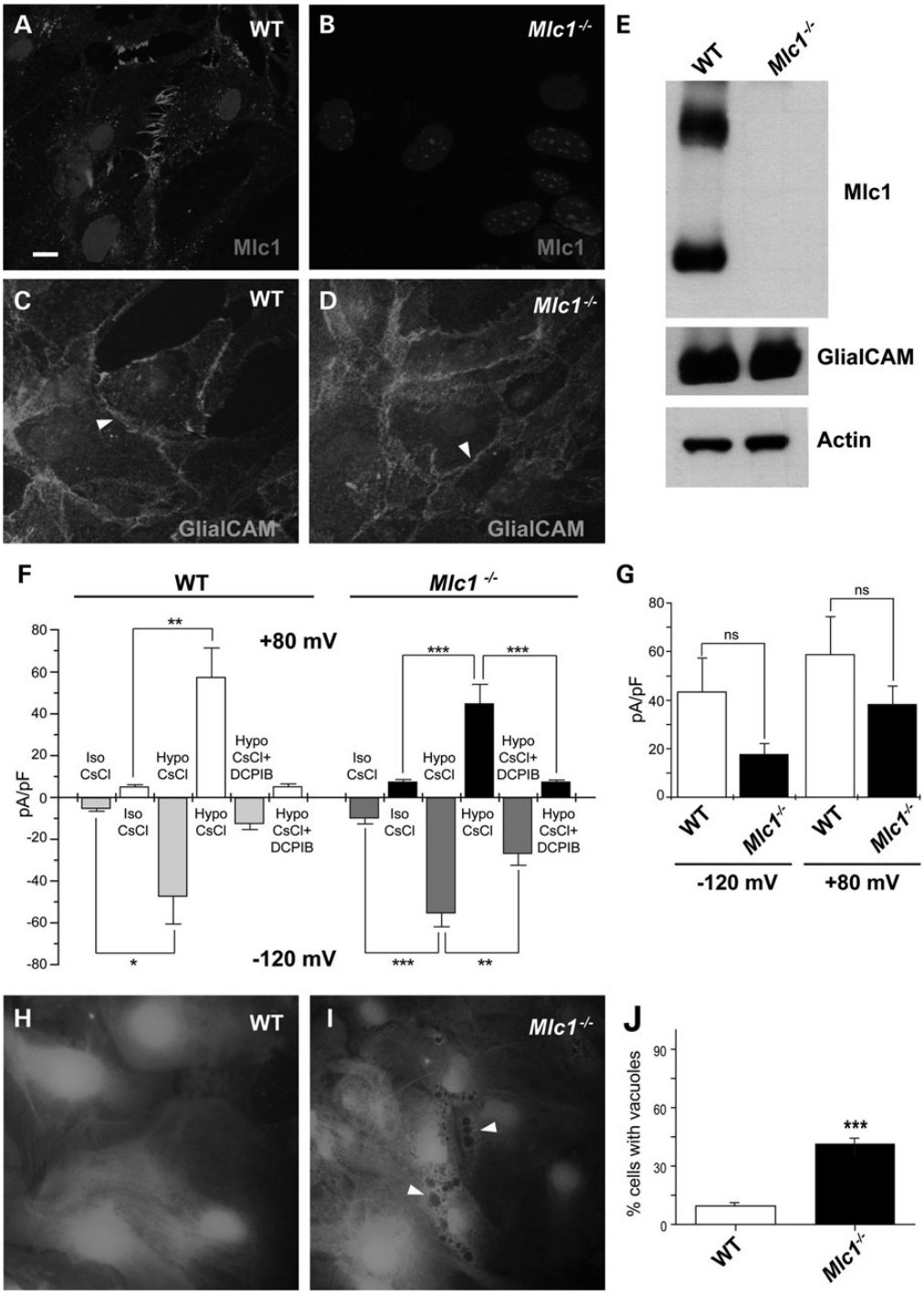

Figure 8. Cultured *Mlc1*$^{-/-}$ astrocytes do not show mislocalization of Glialcam and still present a VRAC response. (**A** and **B**) Immunofluorescence detection of Mlc1 in cultured astrocytes from newborn pups confirms the absence of the Mlc1 protein in *Mlc1*$^{-/-}$ mice. (**C** and **D**) Immunofluorescence detection of Glialcam in cultured astrocytes from newborn pups shows that Glialcam protein is present in cell junctions in *Mlc1*$^{-/-}$ mice, unlike it is seen *in vivo*. Scale bar: 10 μm. (**E**) Western blot of brain extracts show no difference in Glialcam protein levels between wild-type and *Mlc1*$^{-/-}$ mice. (**F** and **G**) Depression of the hypotonicity-evoked chloride current with the Volume Regulated Anion Channel (VRAC) inhibitor DCPIB in wild-type (WT) and *Mlc1*$^{-/-}$ mouse cultured astrocytes. (F) Bar graph of membrane current densities (mean ± SEM) at +80 mV (upper bars) and −120 mV (lower bars) measured in isotonic (Iso CsCl) and hypotonic conditions (Hypo CsCl) and after addition of DCPIB (10 μM) to the hypotonic solution (Hypo CsCl + DCPIB) in wild-type ($n = 9$) and *Mlc1*$^{-/-}$ ($n = 17$) astrocytes. Statistical significance was calculated using paired two-tailed Student's *t*-test; $^{*}P < 0.05$, $^{**}P < 0.01$, $^{***}P < 0.001$. (G) Bar graph of DCPIB-sensitive currents (mean ± SEM) induced by hypotonic challenge at −120 and +80 mV in wild-type ($n = 7$) and *Mlc1*$^{-/-}$ ($n = 7$) mouse astrocytes. Differences in current densities were not significant (ns). (**H** and **I**) Typical pictures of astrocytes obtained from wild-type (H) and *Mlc1*$^{-/-}$ (I) mice. Arrowheads point to vacuoles observed mostly in *Mlc1*$^{-/-}$ astrocytes. (**J**) Quantification of the number of cells containing vacuoles. A cell was positive for vacuolation if have at least three vacuoles of a size bigger than 0.5 μm. Scale bar: 10 μm.

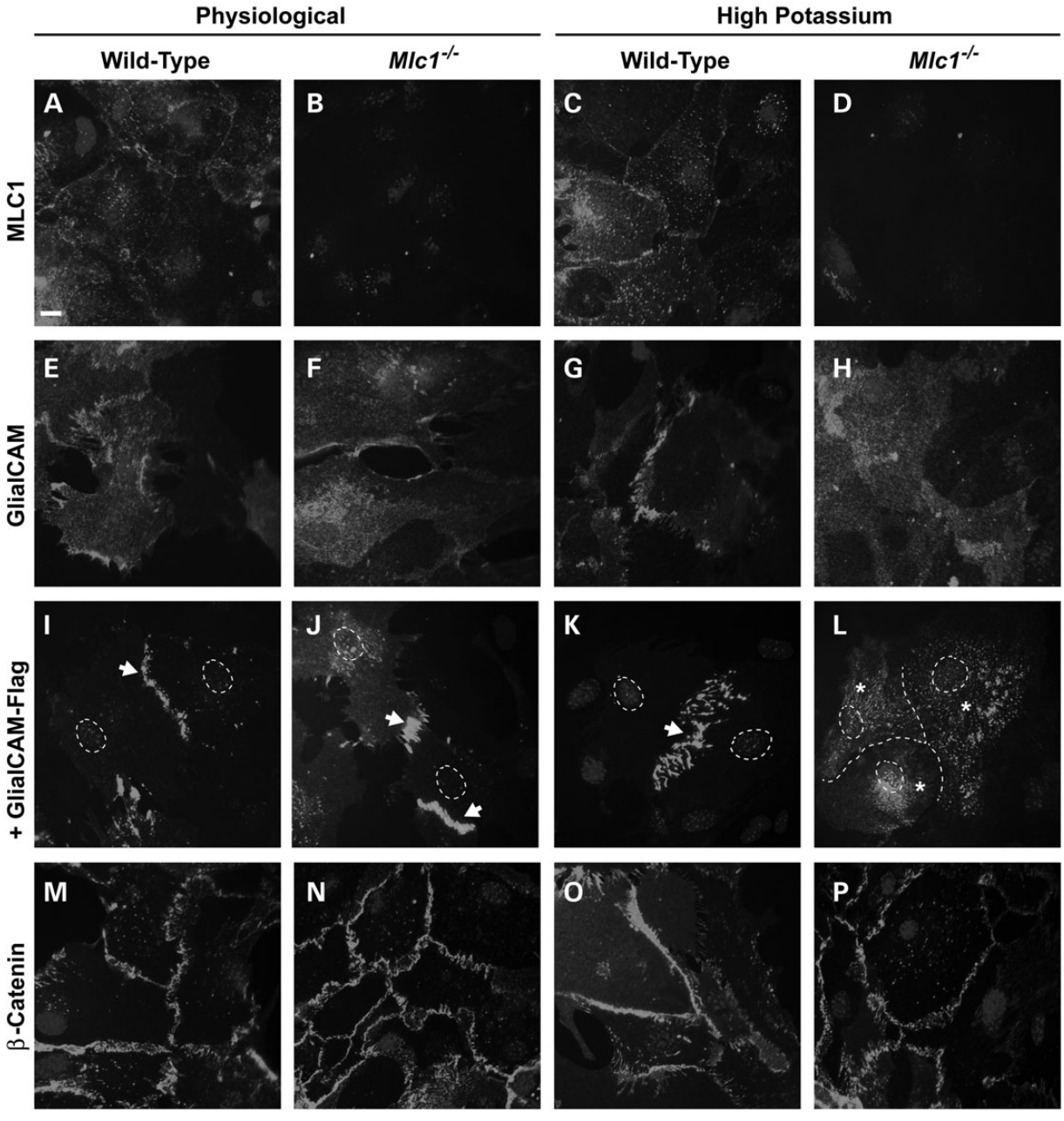

Figure 9. Glialcam localization to astrocyte junctions depends on Mlc1 and the presence of high extracellular potassium concentration. (**A**–**D**) Mlc1 localization in cell junctions in cultured mouse astrocytes do not change between physiological conditions or high extracellular potassium exposure. Scale bar: 10 μm. (**E**–**H**) Glialcam localization in cell junctions in cultured mouse astrocytes is lost when *Mlc1*$^{-/-}$ astrocytes are subjected to 6 h treatment with high extracellular potassium. Four independent experiments gave similar results. (**I**–**L**) Adenoviral-mediated expression of human Flag-tagged GLIALCAM in wild-type and *Mlc1*$^{-/-}$ cultured mouse astrocytes confirms the effect of the high extracellular potassium concentration on GlialCAM localization in cell junctions (arrows) in the absence of Mlc1, when it is found almost exclusively in the cytoplasm (asterisks). Dotted line in (L) labels the junctions between three adjacent astrocytes. Four independent experiments gave similar results. (**M**–**P**) High extracellular potassium concentration does not alter of the localization of a control junctional protein (β-catenin) in cultured mouse astrocytes.

DISCUSSION

We have analysed two animal models (zebrafish, mice) lacking MLC1 protein and compared them with a brain biopsy from an MLC patient. In all cases, localization of GlialCAM at cell junctions is abolished by lack of MLC1. In cultured mouse astrocytes from *Mlc1*$^{-/-}$, this effect is only observed when mimicking neuronal activity.

Despite the fact that *Mlc1* is one of the most astrocyte-specific genes (36,37) and its mutation leads to MLC (3), its precise function is still unknown. As MLC1 is a membrane protein with low homology to ion channels, a possible role as a channel or transporter has been suggested (6). However, no such function has been found so far. RNA interference experiments of *Mlc1* in cultured astrocytes indicated that it may be a component or regulator of VRAC (14,15). Here, we demonstrate that VRAC activity is

still present in the absence of Mlc1. We conclude that MLC1 may affect VRAC activity in an indirect manner and is not a molecular component of VRAC. In agreement with this hypothesis, very recently it has been demonstrated that VRAC activity is mediated by LRRC8 heteromers (38,39). Further work will be needed to define the biochemical relationship between MLC1/GlialCAM and LRRC8 proteins.

Further insight into MLC1 biology came from the finding that another MLC-causing gene, which encodes the cell adhesion molecule GLIALCAM (4), is necessary for stabilizing and targeting MLC1 to astrocyte junctions (4,15). In contrast, GLIALCAM targeting *in vitro* was independent of MLC1 (19,13). However, recent work performed with *Mlc1*$^{-/-}$ and *GlialCAM*$^{-/-}$ mice demonstrated that both mutants reproduce MLC symptoms and that Mlc1 is necessary for GlialCAM localization (22).

We decided to expand the repertoire of MLC animal models to solve this contradiction. We have characterized the orthologues of *MLC1* and *GLIALCAM* in zebrafish. The zebrafish (and other teleost fishes) genome contains two *glialcam* paralogues of which only *glialcama* behaves as mammalian *Glialcam* in terms of subcellular localization and modulation of the chloride channel ClC-2 (24). Both mlc1 and glialcama show a similar expression pattern in the brain as murine Mlc1 and Glialcam (4). mlc1 and glialcama are localized to glial cells especially around brain barriers, radial glia processes and end-feet, and also in Müller glia of the retina.

We have generated a zebrafish line carrying a mutation in *mlc1* that abrogates its protein expression. However, the conservation of *mlc1* in zebrafish does not translate into a severe MLC-like phenotype. We could only detect minor lesions and megalencephaly in the brain of *mlc1*$^{-/-}$ zebrafish by MRI, but not myelin vacuolization even in fish older than 1 year. Although in humans MLC is evident during the first year of life (1), mouse knockout models of both *Glialcam* and *Mlc1* did not present vacuolization during their firsts months of life (22). This difference could reflect their heterochrony of myelination, and that MLC manifests when myelination is at its highest level (1). Zebrafish show regular compact myelin (40), but protein composition differs: P_0 is the major component of CNS myelin, rather than PLP, like in mammals (41). In the transition from an aquatic to a terrestrial environment, there was a switch from P_0 to PLP as the major CNS myelin protein, which provided more neuroprotection (42). Myelination in zebrafish larvae starts at 3 days post-fertilization (dpf), and *myelin basic protein* expression increases at least till 29 dpf (43), but new myelin deposition has been reported in trout even older than 1 year (44). Another significant difference with mammalian brains is the capacity of the adult zebrafish brain for neurogenesis (45) and even repair after injury (46). This is linked to the capacity for re-myelination (47,48). Therefore, it is possible to speculate that zebrafish are able to repair myelin sheath damage produced by the lack of mlc1 protein, so vacuolization never reaches a detectable stage by means of histological methods.

Absence of mlc1 in zebrafish brain leads to the misslocalization of glialcama, as we observed in *Mlc1*$^{-/-}$ mice. This prompted us to re-examine a human MLC biopsy. We found similar results in the cerebellum of the MLC patient. Thus, the reciprocal relationship between MLC1 and GlialCAM for their correct membrane localization has been conserved throughout evolution. This relationship also explains the fact that mutations in either *MLC1* or *GLIALCAM* cause a similar phenotype in MLC1 and MLC2A patients (21).

It has been well described that MLC1 depends on GLIALCAM for exiting the endoplasmatic reticulum and reaching its junctional localization (15). However, a question remains: why does GLIALCAM mislocalize in the absence of MLC1 *in vivo*? We believe that MLC1 is not working as a chaperone of GLIALCAM, as GLIALCAM *in vitro* is able to traffic to cell junctions in the absence of MLC1. In agreement with this hypothesis, GlialCAM mislocalization in *Mlc1*$^{-/-}$ astrocytes in culture only appeared when mimicking neuronal activity by an increase in extracellular potassium. Thus, differences between *in vivo* and *in vitro* effects of MLC1 on GlialCAM localization may be due to the presence of interacting molecules *in vivo* that are not present in culture.

We also suggest that GlialCAM/MLC1 may have a role in the process of potassium siphoning by glial cells. As a result of neuronal electrical activity, potassium is released in order to repolarize the membrane potential, and this excess of potassium needs to be disposed of in a process known as 'potassium siphoning' (49). Glial cells surrounding neurons take up potassium by Kir4.1 channels and then transfer it through Connexin junctions to the astrocytic end-feet surrounding blood vessels, where it is eliminated. Ablation of Kir4.1 (50) or Connexins 32 and 47 (51) results in leukodystrophy characterized by water accumulation in myelin. Work with *Mlc1*$^{-/-}$, *GlialCAM*$^{-/-}$ and *Clcn2*$^{-/-}$ mice models (22,60) and the identification of mutations in *CLCN2* in human patients with leukodystrophy (26) have suggested that the chloride channel ClC-2 may also have a role in potassium-coupled chloride influx. In this sense, GlialCAM changes the rectification of the ClC-2 channel (24), allowing chloride influx at depolarized voltages. Interestingly, new studies with ClC-2 from *C. elegans* have also shown that the primary role of ClC-2 is to mediate chloride influx but not efflux (52). Unfortunately, the precise role of MLC1 in this process is still not known. However, based on these studies, we can speculate that it may have a regulatory role controlling the surface expression of GLIALCAM, which may be needed to regulate in turn the activity of CLC-2. Possibly, the severity of the phenotype caused by the depletion of Mlc1 from fish to mouse and human could be explained based on differences in neuronal activity between species, making Mlc1 or Glialcam more necessary to keep ionic homeostasis in the possibly more active human CNS.

In summary, our work show that the functional relationship between the two proteins causing MLC in vertebrates is evolutionary conserved. We have also increased the diversity of vertebrate animal models for this disease that can offer further insights into the molecular interactions between these two proteins. Our work also explains the similarity of phenotypes caused by mutations in either gene. More importantly, we uncovered a role for MLC1 in GlialCAM localization at astrocyte junctions in the presence of neuronal activity, offering new mechanistic insights into the pathophysiology of MLC.

MATERIALS AND METHODS

Zebrafish maintenance

AB or AB/TL strains were used in all the experiments. Adult fish were maintained in the animal facility at the University of

Barcelona, School of Medicine in Bellvitge Campus, under the standard culture conditions: 28°C, 14 h/10 h light/dark period (53). All experimental procedures conformed to the European Community Guidelines on Animal Care and Experimentation and were approved by animal care and use committees.

The *mlc1*^{fh328} allele was obtained from the laboratory of Dr Cecilia Moens, as a result of an ENU-based TILLING screening (62). The mutant line was generated in an *islet1::GFP* background, which was eliminated by out-crossing to AB wild-type fish. Similarly, two other embryonic recessive lethal phenotypes that were not linked to *mlc1*^{fh328} were eliminated by pair-wise mating and out-crossing. The *mlc1*^{fh328} mutation is a T/G transversion in *mlc1* exon 3 that generates a novel *Dde*I restriction site (CTNAG), which was used for genotyping after amplifying the corresponding fragment of genomic DNA by PCR. The following oligonucleotides were used: TAAATGTGTCTATCTG TATCTGACCGTCAG (underlined is a mutation introduced to eliminate an endogenous *Dde*I restriction site, 16 nucleotides upstream from the *Dde*I restriction site generated by the mutation) and TACTCTGCAAGCCAAAAGCA. Genomic DNA was obtained from tail clipping and extraction by Nucleo Spin Tissue kit (Macherey-Nagel).

Mlc1 knockout mice

Mlc1$^{-/-}$ mice were generated by ICS (Institut Clinique de la Souris, Strasbourg, France) as described previously (22).

Human samples

The MLC patient sample analysed here was already reported (13). Briefly, she carried a homozygous mutation in the *MLC1* gene, resulting in an amino acid change (p.S69L) that leads to the reduced stability of the MLC1 protein and its practical absence.

Molecular biology

Plasmids used were constructed using standard molecular biology techniques employing recombinant PCR and the Multisite Gateway system (Invitrogen). The integrity of all cloned constructs was confirmed by DNA sequencing. For localization studies in HeLa cells, proteins were C-terminally fused to the FLAG epitope or HA-tagged and cloned into the pcDNA3 vector (Invitrogen).

RT-PCR

Adult zebrafish were euthanized using an overdose of tricaine (MS222, Sigma), and tissues were quickly dissected and flash-frozen in liquid nitrogen. Total RNA was isolated with TRIZOL (Life Technologies) and retro-transcribed (RT-PCR) using random hexamers with SuperScript III system (Life Technologies). The following oligonucleotides pairs were used for qPCR: GCACGTTCAGTGGACAACTG and CACAATCATT GGGCCTTCAG (*mlc1*), CCCACCCACCAAGACTAAGC and CATCCTCAGTCGTGCTCATCTG (*glialcama*), and as internal controls (54): CTGGAGGCCAGCTCAAACAT and ATCAAGAAGAGTAGTACCGCTACCATTAC (*ef1a*), TCT GGAGGACTGTAAGAGGTATGC and AGACGCACAATC TTGAGAGCAG (*rpl13a*). qPCR was performed with SYBR Select reagent (Life Technologies) in a StepOne apparatus (Life Technologies). The expression levels were calculated using the comparative C_t method normalized to the internal control genes. The final results were expressed as the relative RNA levels as indicated in the corresponding figures, taking into account the efficiency of each primer pair with the Pfaffl method (55).

Generation of custom antibodies against zebrafish proteins

Immune sera against synthetic peptides from zebrafish mlc1 (QREEASAQEVFSYAQMST, corresponding to amino acids 2–19, in green in Supplementary Material, Fig. S1B) and zebrafish glialcama (EDPPTDGENTMHHHSLPR, corresponding to amino acids 405–422, in green in Supplementary Material, Fig. S2B) were raised in rabbits using the services provided by Eurogentec. The peptide was coupled to keyhole limpet haemocyanin via a cysteine residue that has been added to the N-terminal end of the peptide for mlc1 and to the C-terminal of the peptide for glialcama. After four boosts of immunization, the antisera were affinity purified using the peptide covalently coupled to Sulpholink (Pierce). The polyclonal antibodies were tested by immunoblotting and immunofluorescence on HeLa cells expressing mlc1 or glialcama and on zebrafish brain tissue.

Cell culture and immunofluorescence microscopy

HeLa cells were grown on DMEM containing 10% (v/v) fetal bovine serum (Sigma) and 1% penicillin/streptomycin at 37°C in a humidity controlled incubator with 10% CO_2. Cells were cultured and transfected with the Transfectin reagent (BioRad). Twenty-four hours after transfection, the cells were splitted and transferred into glass-covered petri dishes in which experiments were performed after further 24–48 h. To detect expressed proteins, immunofluorescence staining of cells was performed. They were fixed with phosphate-buffered saline (PBS) containing 3% paraformaldehyde for 15 min, blocked and permeabilized with 10% FBS and 0.1% Triton X-100 in PBS for 2 h at room temperature (RT). Primary antibodies were diluted in the same solution and incubated overnight at 4°C. Cells were washed and incubated for 2 h at RT with secondary antibodies. Cover slips were mounted in Vectashield medium (Vector Laboratories) with 1.5 μg/ml DAPI (Sigma) and visualized using an Olympus DSU spinning disk confocal.

Images were analysed using ImageJ. Pairs of cells were analysed manually and quantified as being in junctions or not being in junctions (around the plasma membrane or intracellular). Intensity profile analysis was used to discern the localization.

Histological staining methods

For immunofluorescence in zebrafish, individuals were deeply anaesthetized in 0.1% tricaine (MS222, Sigma) in fresh water, and then transcardiacally perfused with 4% paraformaldehyde. Fish heads were post-fixed for 24 h at RT. Then brains and eyes were dissected out, cryoprotected and frozen with liquid

nitrogen-cooled methylbutane. Transverse sections (12 μm thick) were cut on a cryostat and mounted onto gelatinized slides.

Sections were rinsed in PBS and pre-incubated with normal goat serum (Sigma, 1:100) for 1 h. Next, they were incubated with a primary antibody or a cocktail of primary antibodies overnight at room temperature. Antibody dilutions used were: rabbit anti-zebrafish mlc1, 1:100; rabbit anti-zebrafish glialcama, 1:100; mouse anti-gfap (ZIRC), 1:500; rat anti-GFP (Nacalai Tesque), 1:1000. After PBS washes, sections were incubated with secondary fluorescent antibodies (Alexa Fluor 488 or 568, 1:500, Invitrogen) for 1 h. After additional PBS washes, sections were mounted using the glycerol-based mounting medium.

For haematoxylin–eosin staining, we used paraffin sections from tissue fixed in Bouin's fixative. Sections were de-waxed and stained using Meyer's haematoxylin followed by eosin. Sections were dehydrated and mounted for imaging.

Zebrafish sections were observed and photographed either under a laser scanning confocal microscope (Nikon A1R) or a bright-field microscope (Nikon E100). Images were adjusted for brightness and contrast with Adobe Photoshop or Corel Photopaint, and they were assembled with Adobe Illustrator.

Human samples were processed and analysed as described previously (13).

Electron microscopy

For electron immunogold experiments, small samples of brain mice tissue were obtained and fixed in 4% paraformaldehyde and 0.1% glutaraldehyde in 0.12 M phosphate buffer, and processed. They were cryoprotected gradually in sucrose and cryofixed by immersion in liquid propane. Freeze substitution was performed at −90°C during 3 days in an Automatic Freeze Substitution System (AFS, Leica); methanol containing 0.5% uranylacetate was used as a substitution medium. Infiltration was carried out in Lowicryl HM20 at −50°C and then polymerized with UV light. Ultrathin sections were collected, and when needed, processed for post embedding immunostaining. For immunostaining, grids were incubated with rabbit anti-Mlc1 (1:10) or mouse anti-GlialCAM (1:10) antisera. The binding of the primary antibody was visualized by incubating with a secondary antibody conjugated to 18 nm gold particles (British BioCell, International). Ependymal cells were recognized by their epithelial location, presence of microvilli and cilia, and high density of organelles in the cytoplasm. Astrocytic processes showed a cytoplasm light appearance with the presence of some fibrils and a very few number of organelles (56).

For electron microscopy of zebrafish myelin sheaths, zebrafish were anaesthetized and transcardially perfused using 4% paraformaldehyde and 0.1% glutaraldehyde in 0.1 M cacodylate buffer with 0.5% calcium chloride. Small pieces of tissue were post-fixed in the same fixative (2 h) and then in 1% osmium tetroxide—with 1.5% potassic ferrocyanide (2 h). Tissue was then dehydrated and included in an epoxy resin. Semithin and thin sections were obtained using an ultramicrotome, mounted and imaged in an electron transmission microscope.

Astrocyte cultures from wild-type and Mlc1$^{-/-}$ mice

Mouse astrocyte cultures were performed as previously described from P0 to P2 mouse pups of the corresponding genotype (16). Calcein stainings were performed by treating the astrocytes with Calcein-AM 2 μM (Life Technologies) for 10 min and then with physiological solution (122 mM NaCl, 3.3 mM KCl, 0,4 mM $MgSO_2$, 1.3 mM $CaCl_2$, 1.2 mM KH_2PO_4, 25 mM Hepes, 10 mM glucose, pH 7.2, 300 mOsm/kg). In some experiments, astrocytes were treated for 6 h with physiological solution or high potassium medium (60 mM NaCl, 60 mM KCl, 0.4 mM $MgSO_2$, 1.3 mM $CaCl_2$, 1.2 mM KH_2PO_4, 25 mM Hepes, 10 mM glucose, pH 7.2, 300 mOsm/kg), to mimic neuronal activity. Then, they were fixed in 4% PFA and processed for immunofluorescence as described above.

Mouse magnetic resonance imaging

Mouse MRI experiments were conducted on a 7.0T BioSpec 70/30 horizontal animal scanner (Bruker BioSpin), equipped with a 12 cm inner diameter actively shielded gradient system (400 mT/m) in at least seven animals of the same age. Receiver coil was a phased array surface coil for mouse brain. Animals were placed in a supine position in a Plexiglas holder with a nose cone for administering anaesthetic gases (isofluorane in a mixture of 30% O_2 and 70% CO_2), fixed using a tooth bar, ear bars and adhesive tape. Tripilot scans were used for accurate positioning of the animal's head in the isocentre of the magnet.

High-resolution T_2-weighted images were acquired by using TurboRARE (rapid acquisition with rapid enhancement) sequence applying repetition time of 2969 ms, echo time of 36 ms, RARE factor = 8, 10 averages, slice thickness = 0.3 mm, number of slices = 25 for horizontal view, 25 coronal slices, field of view = 25 × 25 mm, matrix size = 240 × 240 pixels, resulting in a spatial resolution of 0.104 × 0.104 mm in 0.3 mm slice thickness.

T_2 relaxometry maps were acquired with multislice-multiecho (MSME) sequence by applying 16 different TEs, from 11 to 176 ms, TR = 4764 ms, slice thickness = 0.5 mm, number of coronal slices = 18, FOV = 20 × 20 mm and matrix size = 256 × 256 pixels, resulting in a spatial resolution of 0.078 × 0.078 mm in 0.5.00 mm slice thickness.

Zebrafish magnetic resonance imaging

Magnetic resonance microimaging (μMRI) of zebrafish was performed on a vertical wide-bore 9.4T Bruker Avance 400WB spectrometer, with a 1000 mT/m actively shielded imaging gradient insert (Bruker Biospin GmbH). A birdcage RF coil with an inner diameter 1 cm was used for excitation and detection. The system was interfaced to a Linux PC running Topspin 2.0 and Paravision 5.0 software (Bruker Biospin GmbH). For μMRI, adult zebrafish were euthanized and fixed in 4% buffered paraformaldehyde (Zinc Formal-Fixx, ThermoShandon) for 3 days and subsequently embedded in Fomblin. Before each μMRI measurement, the magnetic field homogeneity was optimized by shimming. Each session of measurements began with a multislice orthogonal gradient-echo sequence for position determination and selection of the desired region for subsequent experiments. High-resolution T_2-weighted imaging was acquired by using TurboRARE (rapid acquisition with rapid enhancement) sequences with echo time (TE) = 10.5 ms; repetition time (TR) = 5000 ms; RARE factor = 4; slice thickness 0.2 mm; number of slices 15; field

of view 12 × 12 mm; image matrix of 256 × 256 pixels, resulting in an in-plane resolution of 47 μm.

T_2 relaxation time measurement in zebrafish brain was performed with MSME sequence by applying eight different TEs (8.5, 17.0, 25.5, 34.0, 42.5, 51.0, 59.5 and 68.0 ms); TR = 1.5 s; slice thickness 0.5 mm; number of slices 6, FOV 12 × 12 mm^2 and matrix size 256 × 256 pixels, resulting in an in-plane resolution of 47 μm. For calculation of T_2 relaxation time, regions of interest (ROIs) were drawn at various locations within the zebrafish brain. Another ROI in the muscle was used as an internal control. Means and standard deviation for T_2 relaxation times for each ROI were calculated.

Two-electrode voltage clamp, western and surface expression in Xenopus oocytes

Xenopus oocytes were injected and maintained as described (57). For rat ClC-2, 10 ng cRNA were injected. When co-expressing, 5 ng cRNA of *glialcama* or *glialcamb* were coinjected with rat ClC-2. Oocytes were perfused with ND96 (in mM): 96 NaCl, 2 KCl, 1.8 $CaCl_2$, 1 $MgCl_2$ and 5 HEPES/TRIS (pH 7.4). To estimate the specific ClC-2-mediated chloride currents, iodide (80 mM NaI replacing the NaCl), which blocks ClC-2-mediated outward currents (58), was applied in every experiment. Oocytes that did not exhibit a significant block were discarded. Currents were measured using a TEC-05X voltage amplifier and the CellWorks program (npi).

Western blot experiments and surface expression in oocytes were performed similarly as previously described (6).

Zebrafish electroretinogram recordings

ERGs were performed at 1-month and 2-month-old young adults (at least five animals). The young adults were anaesthetized by fish system water containing 0.75 mM 3-aminobenzoic acid methyl ester (MESAB, Sigma-Aldrich) and 4.6 mM $NaHCO_3$ before recording. All the experiments were performed at room temperature (20°C).

Fish were dark adapted for at least 30 min and then were placed on the filter paper in the middle of a plastic recording chamber which was filled by 1% agarose. The reference electrode was inserted into the agarose. After the fish was moisturized by a drop of Ringeŕs solution (111 mM NaCl, 2.5 mM KCl, 1 mM $CaCl_2$, 1.6 mM $MgCl_2$, 10 μm EDTA, 10 mM glucose and 3 mM HEPES buffer, adjusted to pH 7.7–7.8 with NaOH), the eye was removed by a loop made of tungsten wire. The loop was placed behind the eye and was pressed down to cut the optic nerve. Meanwhile forceps were used to pull the body and discard it. The isolated eye was then positioned to face the light source (ZEISS XBO 75 W). The recording electrode, filled with Ringer's solution, was placed against the centre of the cornea. All these pre-recording steps were done under dim red illumination. Stimulation light intensity was 6000 lux and attenuated by neutral density filters. Stimulus duration was 100 ms and delivered 50 ms after the recording began. Electronic signals were amplified 1000 times by a pre-amplifier (P55 A.C. Preamplifier, Astro-Med. Inc, Grass Technology) with a band pass between 0.1 and 100 Hz, digitized by DAQ Board NI PCI-6035E (National Instruments) via NI BNC-2090 accessories and displayed via self-developed NI Labview program (59). All the figures were prepared by Origin (Microcal Software).

Mouse electroretinogram recording

The mice were dark-adapted overnight before ERG recording. Under dim red light (λ > 600 nm), the mice were anaesthetized with an i.p. injection of a solution of ketamine (70 mg/kg, Ketolar®, Parke-Davies, S.L.) and xylazine (10 mg/kg, Rompún®) and kept on a heating pad to maintain normal body temperature at 37°C. A topical drop of 1% tropicamide (Colicursí Tropicamida 1%®; Alcon-Cusí, S.A.) were applied to the eyes of the experimental animals before ERG testing. Electrical responses were obtained with Burian-Allen electrodes (Hansen Labs) positioned on the cornea. A drop of methylcellulose (Methocel 2%®; Novartis Laboratories CIBA Vision) was positioned on the cornea to improve electrical conductivity. The reference electrode was placed in the mouth, and the ground electrode at the base of the tail. After positioning the electrodes, the mice were placed in a Ganzfeld stimulator. Stimulation flashes were provided by a Ganzfeld dome light source, which ensured a uniform illumination of the retina and provided a wide range of light intensities. Electrical signals generated in the retina were amplified (×1000) and band filtered between 0.3 and 1000 Hz, using a Grass amplifier (CP511 AC amplifier, Grass Instruments). Electrical signals were digitized at 20 kHz, using a Power Lab data acquisition board (AD Instruments) and displayed on a PC computer monitor. The ERG responses were elicited by stimulation of the retina with light intensities ranging between 10^{-4} and 10^2 cd/s/m^{-2}. A series of ERG responses were averaged (≈20 ERG traces) for each light intensity, after adjusting the time interval between flashes to ensure complete recovery of the response. Standard ERG waves were recorded according to the method recommended by the International Society for Clinical Electrophysiology of Vision (ISCEV).

Electrophysiological measurements on mouse astrocytes

Electrophysiological measurements were performed with the whole-cell configuration of the patch-clamp technique as previously described (60). Briefly, pipette had a resistance of 2–4 MΩ when filled with the intracellular solution. Membrane currents were amplified (amplifier List EPC-7) filtered at 2 kHz (−3 dB) and acquired at a sample rate of 5 kHz on a microcomputer for off-line analyses (pClamp 6, Axon Instruments and Origin 6.0, MicroCal). The access resistance (below 10 MΩ) was corrected for 60–80%. Current densities were calculated by dividing the current values measured at each membrane potential by the cell capacitance estimated from the capacitive transients of the recorded cells corrected by means of the analogical circuit of the patch-clamp amplifier. For the isolation of the Cl^- conductance, the external perfusing saline, called isotonic (Iso CsCl), was (mM): 122 CsCl, 2 $MgCl_2$, 2 $CaCl_2$, 10 TES, 5 glucose, pH 7.4 with CsOH and osmolality ∼320 mOsm with mannitol. The intracellular (pipette) solution was composed of (mM): 126 CsCl, 2 $MgCl_2$, 1 EGTA, 10 TES, pH 7.2 and osmolality ∼300 mOsm with mannitol. Hypotonic extracellular solution (Hypo CsCl) ∼260 mOsm was obtained by omitting mannitol. Osmolality was measured with a vapour–pressure osmometer (Wescor 5500, Delcon). All salts and various

molecules were from Sigma. The DCPIB was prepared in DMSO at a concentration 1000-fold higher than that used in the perfusing saline.

SUPPLEMENTARY MATERIAL

Supplementary Material is available at *HMG* online.

ACKNOWLEDGEMENTS

We thank Marisol Montolio and Hernan López-Schier for their help in the initial stages of the project, Esther Prat and Laura González for the management of the *Mlc1* colony, Lara Sedó and Beatriz Gamarra for excellent fish care, Verónica López-Guillín and Catalina Sueiro for assistance with electron microscopy and histology and Lupe Soria for mice MRI. We also thank Thomas J Jentsch and Ian Orozco for critical reading of the article. We also thank IDIBELL and Alvaro Gimeno (Estabulari Bellvitge) for their help to setup the zebrafish facility.

Conflict of Interest statement. None declared.

FUNDING

This work was supported in by SAF 2009-07014 (R.E.) and SAF2012-31486 (R.E.), PS09/02672-ERARE to R.E., ELA Foundation 2009-017C4 and 2012-014C2B project (R.E. and V.N.), 2009 SGR 719 (R.E.), SAF 2009-12606-C02-02 (V.N.), 2009 SGR01490 (V.N.). R.E. is a recipient of an ICREA Academia prize.

REFERENCES

1. Van der Knaap, M.S., Boor, I. and Estevez, R. (2012) Megalencephalic leukoencephalopathy with subcortical cysts: chronic white matter oedema due to a defect in brain ion and water homoeostasis. *Lancet Neurol.*, **11**, 973–985.
2. Van der Knaap, M.S., Valk, J., Barth, P.G., Smit, L.M., van Engelen, B.G. and Tortori Donati, P. (1995) Leukoencephalopathy with swelling in children and adolescents: MRI patterns and differential diagnosis. *Neuroradiology*, **37**, 679–686.
3. Leegwater, P.A., Yuan, B.Q., van der Steen, J., Mulders, J., Konst, A.A., Boor, P.K., Mejaski-Bosnjak, V., van der Maarel, S.M., Frants, R.R., Oudejans, C.B. *et al.* (2001) Mutations of MLC1 (KIAA0027), encoding a putative membrane protein, cause megalencephalic leukoencephalopathy with subcortical cysts. *Am. J. Hum. Genet.*, **68**, 831–838.
4. Lopez-Hernandez, T., Ridder, M.C., Montolio, M., Capdevila-Nortes, X., Polder, E., Sirisi, S., Duarri, A., Schulte, U., Fakler, B., Nunes, V. *et al.* (2011a) Mutant GlialCAM causes megalencephalic leukoencephalopathy with subcortical cysts, benign familial macrocephaly, and macrocephaly with retardation and autism. *Am. J. Hum. Genet.*, **88**, 422–432.
5. Boor, P.K., de Groot, K., Waisfisz, Q., Kamphorst, W., Oudejans, C.B., Powers, J.M., Pronk, J.C., Scheper, G.C. and van der Knaap, M.S. (2005) MLC1: a novel protein in distal astroglial processes. *J. Neuropathol. Exp. Neurol.*, **64**, 412–419.
6. Teijido, O., Martinez, A., Pusch, M., Zorzano, A., Soriano, E., Del Rio, J.A., Palacin, M. and Estevez, R. (2004) Localization and functional analyses of the MLC1 protein involved in megalencephalic leukoencephalopathy with subcortical cysts. *Hum. Mol. Genet.*, **13**, 2581–2594.
7. Teijido, O., Casaroli-Marano, R., Kharkovets, T., Aguado, F., Zorzano, A., Palacin, M., Soriano, E., Martinez, A. and Estevez, R. (2007) Expression patterns of MLC1 protein in the central and peripheral nervous systems. *Neurobiol. Dis.*, **26**, 532–545.
8. Van der Knaap, M.S., Barth, P.G., Vrensen, G.F. and Valk, J. (1996) Histopathology of an infantile-onset spongiform leukoencephalopathy with a discrepantly mild clinical course. *Acta Neuropathol.*, **92**, 206–212.
9. Leegwater, P.A., Boor, P.K., Yuan, B.Q., van der Steen, J., Visser, A., Konst, A.A., Oudejans, C.B., Schutgens, R.B., Pronk, J.C. and van der Knaap, M.S. (2002) Identification of novel mutations in MLC1 responsible for megalencephalic leukoencephalopathy with subcortical cysts. *Hum. Genet.*, **110**, 279–283.
10. Montagna, G., Teijido, O., Eymard-Pierre, E., Muraki, K., Cohen, B., Loizzo, A., Grosso, P., Tedeschi, G., Palacin, M., Boespflug-Tanguy, O. *et al.* (2006) Vacuolating megalencephalic leukoencephalopathy with subcortical cysts: functional studies of novel variants in MLC1. *Hum. Mutat.*, **27**, 292.
11. Wang, J., Shang, J., Wu, Y., Gu, Q., Xiong, H., Ding, C., Wang, L., Gao, Z., Wu, X. and Jiang, Y. (2011) Identification of novel MLC1 mutations in Chinese patients with megalencephalic leukoencephalopathy with subcortical cysts (MLC). *J. Hum. Genet.*, **56**, 138–142.
12. Duarri, A., Teijido, O., Lopez-Hernandez, T., Scheper, G.C., Barriere, H., Boor, I., Aguado, F., Zorzano, A., Palacin, M., Martinez, A. *et al.* (2008) Molecular pathogenesis of megalencephalic leukoencephalopathy with subcortical cysts: mutations in MLC1 cause folding defects. *Hum. Mol. Genet.*, **17**, 3728–3739.
13. Lopez-Hernandez, T., Sirisi, S., Capdevila-Nortes, X., Montolio, M., Fernandez-Duenas, V., Scheper, G.C., van der Knaap, M.S., Casquero, P., Ciruela, F., Ferrer, I. *et al.* (2011b) Molecular mechanisms of MLC1 and GLIALCAM mutations in megalencephalic leukoencephalopathy with subcortical cysts. *Hum. Mol. Genet.*, **20**, 3266–3277.
14. Ridder, M.C., Boor, I., Lodder, J.C., Postma, N.L., Capdevila-Nortes, X., Duarri, A., Brussaard, A.B., Estevez, R., Scheper, G.C., Mansvelder, H.D. *et al.* (2011) Megalencephalic leucoencephalopathy with cysts: defect in chloride currents and cell volume regulation. *Brain*, **134**, 3342–3354.
15. Capdevila-Nortes, X., López-Hernández, T., Apaja, P.M., López de Heredia, M., Sirisi, S., Callejo, G., Arnedo, T., Nunes, V., Lukacs, G.L., Gasull, X. *et al.* (2013) Insights into MLC pathogenesis: GlialCAM is an MLC1 chaperone required for proper activation of volume-regulated anion currents. *Hum. Mol. Genet.*, **22**, 4405–4216.
16. Duarri, A., Lopez de Heredia, M., Capdevila-Nortes, X., Ridder, M.C., Montolio, M., Lopez-Hernandez, T., Boor, I., Lien, C.F., Hagemann, T., Messing, A. *et al.* (2011) Knockdown of MLC1 in primary astrocytes causes cell vacuolation: a MLC disease cell model. *Neurobiol. Dis.*, **43**, 228–238.
17. Brignone, M.S., Lanciotti, A., Macioce, P., Macchia, G., Gaetani, M., Aloisi, F., Petrucci, T.C. and Ambrosini, E. (2011) The beta1 subunit of the Na,K-ATPase pump interacts with megalencephalic leucoencephalopathy with subcortical cysts protein 1 (MLC1) in brain astrocytes: new insights into MLC pathogenesis. *Hum. Mol. Genet.*, **20**, 90–103.
18. Lanciotti, A., Brignone, M.S., Molinari, P., Visentin, S., De Nuccio, C., Macchia, G., Aiello, C., Bertini, E., Aloisi, F., Petrucci, T.C. *et al.* (2012) Megalencephalic leukoencephalopathy with subcortical cysts protein 1 functionally cooperates with the TRPV4 cation channel to activate the response of astrocytes to osmotic stress: dysregulation by pathological mutations. *Hum. Mol. Genet.*, **21**, 2166–2180.
19. Chung Moh, M., Hoon Lee, L. and Shen, S. (2005) Cloning and characterization of hepaCAM, a novel Ig-like cell adhesion molecule suppressed in human hepatocellular carcinoma. *J. Hepatol.*, **42**, 833–841.
20. Favre-Kontula, L., Rolland, A., Bernasconi, L., Karmirantzou, M., Power, C., Antonsson, B. and Boschert, U. (2008) GlialCAM, an immunoglobulin-like cell adhesion molecule is expressed in glial cells of the central nervous system. *Glia*, **56**, 633–645.
21. Van der Knaap, M.S., Lai, V., Kohler, W., Salih, M.A., Fonseca, M.J., Benke, T.A., Wilson, C., Jayakar, P., Aine, M.R., Dom, L. *et al.* (2010) Megalencephalic leukoencephalopathy with cysts without MLC1 defect. *Ann. Neurol.*, **67**, 834–837.
22. Hoegg-Beiler, M.B., Sirisi, S., Orozco, I., Ferrer, I., Hohensee, S., Auberson, M., Gödde, K., Vilches, C., López de Heredia, M., Nunes, V., Estévez, R. and Jentsch, T. (2014) Disrupting MLC1 GlialCAM and ClC-2 interactions in leukodystrophy entails glial Cl- channel dysfunction. *Nat. Commun*, **5**, 3475.
23. Arnedo, T., Aiello, C., Jeworutzki, E., Dentici, M.L., Uziel, G., Simonati, A., Pusch, M., Bertini, E. and Estévez, R. (2013) Expanding the spectrum of megalencephalic leukoencephalopathy with subcortical cysts in two patients with GLIALCAM mutations. *Neurogenetics*. doi:10.1007/s10048-013-0381-x.
24. Jeworutzki, E., Lopez-Hernandez, T., Capdevila-Nortes, X., Sirisi, S., Bengtsson, L., Montolio, M., Zifarelli, G., Arnedo, T., Muller, C.S., Schulte,

U. *et al.* (2012) GlialCAM, a protein defective in a leukodystrophy, serves as a ClC-2 Cl(−) channel auxiliary subunit. *Neuron*, **73**, 951–961.
25. Maduke, M.C. and Reimer, R.J. (2012) Biochemistry to the rescue: a ClC-2 auxiliary subunit provides a tangible link to leukodystrophy. *Neuron*, **73**, 855–857.
26. Depienne, C., Bugiani, M., Dupuits, C., Galanaud, D., Touitou, V., Postma, N., van Berkel, C., Polder, E., Tollard, E., Darios, F. *et al.* (2013) Brain white matter oedema due to ClC-2 chloride channel deficiency: an observational analytical study. *Lancet Neurol.*, **12**, 659–668.
27. Drumm, M.L., Wilkinson, D.J., Smit, L.S., Worrell, R.T., Strong, T.V., Frizzell, R.A., Dawson, D.C. and Collins, F.S. (1991) Chloride conductance expressed by delta F508 and other mutant CFTRs in Xenopus oocytes. *Science*, **254**, 1797–1799.
28. Lawson, N.D. and Weinstein, B.M. (2002) In vivo imaging of embryonic vascular development using transgenic zebrafish. *Dev. Biol.*, **248**, 307–318.
29. Cuoghi, B. and Mola, L. (2009) Macroglial cells of the teleost central nervous system: a survey of the main types. *Cell Tissue Res.*, **338**, 319–332.
30. Decher, N., Lang, H.J., Nilius, B., Bruggemann, A., Busch, A.E. and Steinmeyer, K. (2001) DCPIB is a novel selective blocker of I(Cl,swell) and prevents swelling-induced shortening of guinea-pig atrial action potential duration. *Br. J. Pharmacol.*, **134**, 1467–1479.
31. Benfenati, V., Nicchia, G.P., Svelto, M., Rapisarda, C., Frigeri, A. and Ferroni, S. (2007) Functional down-regulation of volume-regulated anion channels in AQP4 knockdown cultured rat cortical astrocytes. *J. Neurochem.*, **100**, 87–104.
32. Parkerson, K.A. and Sontheimer, H. (2004) Biophysical and pharmacological characterization of hypotonically activated chloride currents in cortical astrocytes. *Glia*, **46**, 419–436.
33. Clark, S., Jordt, S.E., Jentsch, T.J. and Mathie, A. (1998) Characterization of the hyperpolarization-activated chloride current in dissociated rat sympathetic neurons. *J. Physiol.*, **506**(Pt 3), 665–678.
34. Makara, J.K., Rappert, A., Matthias, K., Steinhauser, C., Spat, A. and Kettenmann, H. (2003) Astrocytes from mouse brain slices express ClC-2-mediated Cl- currents regulated during development and after injury. *Mol. Cell Neurosci.*, **23**, 521–530.
35. Wang, F., Xu, Q., Wang, W., Takano, T. and Nedergaard, M. (2012) Bergmann glia modulate cerebellar Purkinje cell bistability via Ca2+-dependent K+ uptake. *Proc. Natl Acad. Sci. USA*, **109**, 7911–7916.
36. Cahoy, J.D., Emery, B., Kaushal, A., Foo, L.C., Zamanian, J.L., Christopherson, K.S., Xing, Y., Lubischer, J.L., Krieg, P.A., Krupenko, S.A. *et al.* (2008) A transcriptome database for astrocytes, neurons, and oligodendrocytes: a new resource for understanding brain development and function. *J. Neurosci.*, **28**, 264–278.
37. Lovatt, D., Sonnewald, U., Waagepetersen, H.S., Schousboe, A., He, W., Lin, J.H.-C., Han, X., Takano, T., Wang, S., Sim, F.J. *et al.* (2007) The transcriptome and metabolic gene signature of protoplasmic astrocytes in the adult murine cortex. *J. Neurosci.*, **27**, 12255–12266.
38. Voss, F.K., Ullrich, F., Münch, J., Lazarow, K., Lutter, D., Mah, N., Andrade-Navarro, M.A., von Kries, J.P., Stauber, T. and Jentsch, T.J. (2014) Identification of LRRC8 heteromers as an essential component of the volume-regulated anion channel VRAC. *Science*. doi:10.1126/science.1252826.
39. Qiu, Z., Dubin, A.E., Mathur, J., Tu, B., Reddy, K., Miraglia, L.J., Reinhardt, J., Orth, A.P. and Patapoutian, A. (2014) SWELL1, a plasma membrane protein, is an essential component of volume-regulated anion channel. *Cell*, **157**, 447–458.
40. Brosamle, C. and Halpern, M. (2002) Characterization of myelination in the developing zebrafish. *Glia*, **39**, 47–57.
41. Jeserich, G., Klempahn, K. and Pfeiffer, M. (2008) Features and functions of oligodendrocytes an myelin proteins of lower vertebrate species. *J. Mol. Neurosci.*, **35**, 117–126.
42. Yin, X., Baek, R.C., Kirschner, D.A., Peterson, A., Fujii, Y., Nave, K.-A., Macklin, W.B. and Trapp, B.D. (2006) Evolution of a neuroprotective function of central nervous system myelin. *J. Cell Biol.*, **172**, 469–478.
43. Buckley, C.E., Marguerie, A., Alderton, W.K. and Franklin, R.J.M. (2010) Temporal dynamics of myelination in the zebrafish spinal cord. *Glia*, **58**, 802–812.
44. Jeserich, G. (1981) A morphological and biochemical study of myelin of myelinogenesis in fish brain. *Dev. Neurosci.*, **4**, 373–381.
45. Chapouton, P., Jagasia, R. and Bally-Cuif, L. (2007) Adult neurogenesis in non-mammalian vertebrates. *BioEssays*, **29**, 745–757.
46. Kyritsis, N., Kizil, C., Zocher, S., Kroehne, V., Kaslin, J., Freudenreich, D., Iltzsche, A. and Brand, M. (2012) Acute inflammation initiates the regenerative response in the adult zebrafish brain. *Science*, **338**, 1353–1356.
47. Buckley, C.E., Goldsmith, P. and Franklin, R.J.M. (2008) Zebrafish myelination: a transparent model for remyelination?. *Dis. Model. Mech.*, **1**, 221–228.
48. Dubois-Dalcq, M., Williams, A., Stadelmann, C., Stankoff, B., Zalc, B. and Lubetzki, C. (2008) From fish to man: understanding endogenous remyelination in central nervous system demyelinating diseases. *Brain*, **131**, 1686–1700.
49. Rash, J.E. (2010) Molecular disruptions of the panglial syncytium block potassium siphoning and axonal saltatory conduction: pertinence to neuromyelitis optica and other demyelinating diseases of the central nervous system. *Neuroscience*, **168**, 982–1008.
50. Neusch, C., Rozengurt, N., Jacobs, R.E., Lester, H.A. and Kofuji, P. (2001) Kir4.1 potassium channel subunit is crucial for oligodendrocyte development and in vivo myelination. *J. Neurosci.*, **21**, 5429–5438.
51. Menichella, D.M., Majdan, M., Awatramani, R., Goodenough, D.A., Sirkowski, E., Scherer, S.S. and Paul, D.L. (2006) Genetic and physiological evidence that oligodendrocyte gap junctions contribute to spatial buffering of potassium released during neuronal activity. *J. Neurosci.*, **26**, 10984–10991.
52. Branicky, R., Miyazaki, H., Strange, K. and Schafer, W.R. (2014) The voltage-gated anion channels encoded by clh-3 regulate egg laying in *C. elegans* by modulating motor neuron excitability. *J. Neurosci.*, **34**, 764–775.
53. Westerfield, M. (2000) *The Zebrafish Book. A Guide for the Laboratory use of Zebrafish (Danio Rerio)*, University of Oregon Presss, Eugene.
54. Tang, R., Dodd, A., Lai, D., McNabb, W.C. and Love, D.R. (2007) Validation of zebrafish (Danio rerio) reference genes for quantitative real-time RT-PCR normalization. *Acta Biochim. Biophys. Sin. (Shanghai)*, **39**, 384–390.
55. Pfaffl, M.W. (2001) A new mathematical model for relative quantification in real-time RT-PCR. *Nucleic Acids Res.*, **29**, e45.
56. Peters, A., Palay, S.L. and de Webster, H.F. (1991) *The Fine Structure of the Nervous System: The Neurons and Their Supporting Cells*. Saunders Company, Philadelphia, USA.
57. Estevez, R., Schroeder, B.C., Accardi, A., Jentsch, T.J. and Pusch, M. (2003) Conservation of chloride channel structure revealed by an inhibitor binding site in ClC-1. *Neuron*, **38**, 47–59.
58. Thiemann, A., Grunder, S., Pusch, M. and Jentsch, T.J. (1992) A chloride channel widely expressed in epithelial and non-epithelial cells. *Nature*, **356**, 57–60.
59. Rinner, O., Rick, J.M. and Neuhauss, S.C.F. (2005) Contrast sensitivity, spatial and temporal tuning of the larval zebrafish optokinetic response. *Invest. Ophthalmol. Vis. Sci.*, **46**, 137–142.
60. Ferroni, S., Marchini, C., Nobile, M. and Rapisarda, C. (1997) Characterization of an inwardly rectifying chloride conductance expressed by cultured rat cortical astrocytes. *Glia*, **21**, 217–227.
61. Blanz, J., Schweizer, M., Auberson, M., Maier, H., Muenscher, A., Hubner, C.A. and Jentsch, T.J. (2007) Leukoencephalopathy upon disruption of the chloride channel ClC-2. *J. Neurosci.*, **27**, 6581–6589.
62. Wienholds, E., van Eeden, F., Kosters, M., Mudde, J., Plasterk, R.H. and Cuppen, E. (2003) Efficient target-selected mutagenesis in zebrafish. *Genome Res*, **13**, 2700–2707.